OPEN ACCESS

GAVIN PUBLISHERS

Biosensors and Bioelectronics Open Access

Kim YJ, et al. Biosens Bioelectron Open Acc: BBOA-133.

Research Article

DOI: 10.29011/ 2577-2260.100033

Development of *Lactobacillus kimchicus* DCY51T Mediated Gold Nanoparticles for Delivery of Ginsenoside Compound K with Photoluminescence and Internal Reflection Scattering Towards Cancer Cell Lines

Yeon-Ju Kim[1*], Haribalan Perumalsamy[1], Josua Markus[1], Sri Renukadevi Balusamy[2], Chao Wang[1], Seungah Lee[3], Sung Kim[4], Verónica Castro-Aceituno[1], Deok Chun Yang[1]

[1]Department of Oriental Medicinal Biotechnology, College of Life Science, Kyung Hee University, Yongin-si, Gyeonggi-do, Republic of Korea

[2]Department of Food Science and Biotechnology, Sejong University, Gwangjin-gu, Seoul, Republic of Korea

[3]Department of Applied Chemistry and Institute of Natural Sciences, College of Applied Science, Kyung Hee University, Republic of Korea

[4]Center for Global Converging Humanities, Kyung Hee University, Republic of Korea

[*]**Corresponding author:** Yeon-Ju Kim, Department of Oriental Medicinal Biotechnology, College of Life Science, Kyung Hee University, Yongin-si, Gyeonggi-do 446-701, Republic of Korea. Tel: +82312012100; Email: yeonjukim@khu.ac.kr

Citation: Kim YJ, Perumalsamy H, Markus J, Balusamy SR, Wang C, et al. (2018) Development of *Lactobacillus kimchicus* DCY51T Mediated Gold Nanoparticles for Delivery of Ginsenoside Compound K with Photoluminescence and Internal Reflection Scattering Towards Cancer Cell Lines. Biosens Bioelectron Open Acc: BBOA-133. DOI: 10.29011/ 2577-2260.100033

Received Date: 14 April, 2018; **Accepted Date:** 04 May, 2018; **Published Date:** 11 May, 2018

Abstract

Ginsenoside CK has been successfully loaded non-covalently into gold nanoparticles (DCY51^T-AuNps-CK) through one-pot biosynthesis by probiotic *Lactobacillus kimchicus* DCY51^T isolated from Korean kimchi via an intracellular membrane-bound mechanism. The health properties of kimchi, a fermented food from Korea, and its microflora have received much attention in recent years due to their antioxidative and anticancer activity. The ginsenoside-loaded AuNps were characterized by analytical and spectroscopic techniques. *In vitro* DPPH assay revealed that the gold nanoparticles demonstrated potentials as free radical scavengers. Moreover, DCY51^T-AuNps and DCY51^T-AuNps-CK were resistant to aggregation caused by pH variation or a high ionic strength environment. In cancer cell lines, DCY51^T-AuNps-CK exhibited slightly higher cytotoxicity in lung adenocarcinoma cells and colon adenocarcinoma cells than DCY51^T-AuNps. Finally, DCY51^T-AuNps-CK demonstrated increased apoptosis in cancer cells in conjunction with laser therapy probably due to the increased sensitivity of tumor cells to ginsenoside or light-triggered drug release into cancer cells. Thus, we propose that DCY51^T-AuNps-CK can be used as novel photo thermal therapy agents against stomach, colon and lung cancer treatment and to overcome resistance to laser therapy by synergistic chemotherapy effect.

Keywords: Cancer; Drug Delivery; Ginsenoside CK; Gold Nanoparticles; Green Synthesis; *Lactobacillus kimchicus* DCY51^T

Introduction

Panax ginseng Meyer (Korean ginseng) has been regarded as one of the acclaimed herbal medicines for over two thousand years as Chinese traditional medicine [1]. The name "*Panax*" connotes "All-Healing" in Latin and "ginseng" literally translates to "Essence of Men" in Chinese owing to its roots resembling humanoid shape [2,3]. The main bioactive components of ginseng are collectively classified as ginsenosides. They are a group of triterpenoids saponins which were first isolated and identified by Shibata et al. in 1963 [1]. Among these ginsenosides, the metabolites of Protopanaxadiol (PPD)-type ginsenosides are predominantly transformed into Compound K (CK) and ginsenoside Rh2 [1]. These minor ginsenosides (e.g. CK) often exhibit superior pharmacological effects compared to their precursors [1,4]. However, their clinical application is significantly limited due to their hydrophobic saponin backbone, poor bioavailability and

absorption, and non-targeted cytotoxicity to normal cells [5-7]. As a result, biomolecular conjugations of ginsenosides and drug delivery techniques play significant roles to solve these problematic issues.

The objective of this study is to develop gold nanocarriers as ginsenoside delivery agents that may elevate their capacities as effective anticancer agents. Green synthesis of metal nanoparticles is employed to ensure elimination of toxic ligands and augmentation of bioactive enzyme that may render nanocarriers biologically active for biomedical applications. Finally, poorly water soluble ginsenosides (CK) can be delivered by the biosynthesized nanocarriers by loading to the surface of nanoparticles to improve water dispersibility, stability, and therapeutic effect. Gold nanoparticles are specifically designed to work as bio-inert material on normal and cancer cells while excitations by laser at a mild wavelength are expected to induce more apoptosis in cancer cells

Following the synthesis of novel ginsenoside-metal nanocarriers, they will be extensively characterized by spectroscopic and analytical instruments, such as Ultra-Violet Visible (UV-Vis) spectroscopy, Field Emission Transmission Electron Microscopy (FE-TEM), Energy-Dispersive X-Ray (EDX) spectroscopy, elemental mapping, X-Ray Powder Diffraction (XRD), Selected Area Electron Diffraction (SAED), Dynamic Light Scattering (DLS), and Fourier Transform Infrared (FTIR) spectroscopy. Drug loading will be determined by Liquid Chromatography-Mass Spectrometry (LC-MS). Furthermore, the *in vitro* stability of these nanocarriers in a wide range of pH and electrolyte conditions will be assessed. Finally, the *in vitro* photothermal activity of gold nanoparticles will be performed to evaluate the efficacy of ginsenoside conjugation method used to functionalize gold nanocarriers.

Materials and Methods

Materials

L. kimchicus DCY51^T strain was received from Korean Collection for Type Cultures (KCTC 12976^T) with NCBI accession number EU678893. The type strain was previously isolated from kimchi, a fermented vegetable food, collected in Gyeonggi province in South Korea by [8]. MRS (de Man, Rogosa, and Sharpe) broth and agar were purchased from MBcell (Seoul, Republic of Korea). Analytical grade hydrogen tetrachloroaurate (III) hydrate (gold salt) and hydrochloric acid (HCl, ACS reagent, 37%) were purchased from Sigma-Aldrich Chemicals (St. Louis, MO, USA). Sodium chloride (NaCl, ≥99.50%) and sodium hydroxide (NaOH, ≥98%) were purchased from Daejung Chemicals and Metals Co., Ltd. Compound K (CK, ≥90%) was acquired from Ginseng bank, Kyung Hee University (Yongin, Republic of Korea). Pre-made phosphate-buffered saline (20×PBS) was purchased from Biosesang (Seongnam, Republic of Korea). Methyl alcohol (MeOH, 95%) was procured from Samchun Pure Chemical Co. Ltd. (Pyeongtaek, Republic of Korea). Other chemicals were obtained from commercial suppliers and used as received.

Cell Lines

RAW264.7 (murine leukemic macrophage cell line) and A549 cells (human lung adenocarcinoma cell line) were obtained from Korean Cell Line Bank (KCLB, Seoul, Republic of Korea). HT29 (human colorectal adenocarcinoma cell line) and AGS cells (human stomach cancer cell line) were obtained from American Type Culture Collection (ATCC, Manassas, VA, USA). Dulbecco's Modified Eagle Medium (DMEM), Fetal Bovine Serum (FBS), RPMI 1640 culture media, and penicillin-streptomycin solution were purchased from GenDEPOT (Barker, TX, USA). Soluble 3-(4,5-dimethyl-thiazol-2yl)-2, 5-diphenyl tetrazolium bromide (MTT) was purchased from Life technologies (Eugene, OR, USA). Other chemicals were obtained from commercial suppliers and used as received.

Phylogenetic Tree Construction

The type strain was obtained from Korean Collection for Type Cultures (KCTC 12976^T) with NCBI accession number EU678893. The type strain was previously isolated from kimchi, a fermented vegetable food, collected in Gyeonggi province in South Korea by Liang et al. [8]. To construct phylogenetic tree, the 16S rRNA gene sequences of nanoparticle-producing potent strain were sequenced by Genotech (Daejeon, Korea) and related taxa were retrieved from GenBank database and EzTaxon-e server [8]. Multiple alignments of related taxa were organized by ClustalX software [9]. Gaps were edited by BioEdit program (10,11]. Evolutionary distances were calculated using Kimura's two-parameter model [12]. Phylogenetic trees were constructed using neighbor-joining and maximum-parsimony algorithms by MEGA6 program [13]. Bootstrap values were determined on the basis of 1000 replications. Comparison of the 16S rRNA gene sequence of the type strain with 16S rRNA gene sequences of reference strains was achieved using EzTaxon-e server [10,11]. To activate the type strain, the isolated colonies were streaked on MRS (de Man, Rogosa, and Sharpe) agar. The plates were then incubated at 37°C for 48 h and growth was studied [8].

Preparation of DCY51^T- AUNPS and DCY51^T-AUNPS-CK

DCY51^T-AuNps were synthesized by *L. kimchicus* DCY51^T according to a previous method by Markus et al. [14]. Poorly water-soluble CK was loaded into DCY51^T-AuNps by a one-pot synthesis. Following the addition of gold salt solution into the microbial cell suspension in 10 mL PBS (1×) to achieve a concentration of 1

mM, drug solutions containing 1 mg of CK were added into the respective reaction mixtures, incubated at 37°C, and shaken at 150× g under dark conditions. The synthesis of DCY51^T-AuNps-CK was detected by visual inspection for a change in the color of the biomass in the reaction mixtures. Thereafter, the vividly-colored reaction mixtures were centrifuged at 2,500× g for 5 min to remove supernatant and unloaded drugs. To collect the trapped, drug-loaded nanoparticles from the bacterial cells, the pellets underwent alternating cycles of ultra-sonication and continuous centrifugation at 2,500× g for 5 min. Drug-loaded DCY51^T-AuNps were collected by high speed centrifugation at 28,000× g for 10 min and were washed exhaustively with distilled water. Finally, DRUG-LOADED DCY51^T-AUNPS were stored as aqueous suspensions at 4°C until further experiments. Solid specimens were obtained by air-drying nanoparticles overnight.

Characterization of Nanoparticles

Concentration of DCY51^T-AuNps from the drug-loaded nanoparticle suspension was estimated by the equation derived by Haiss et al. whereas the particle diameter was estimated by Debye-Scherrer formula with a shape factor (*K*) of 0.9 [15,16]. The absorbance spectra of the drug-loaded nanoparticle suspension were scanned in the range of 300-800 nm by Ultraviolet-Visible (UV-Vis) spectrophotometer (Ultrospec™ 2100 pro) with a 10 mm path length quartz cuvette (2100 Pro, Amersham Biosciences Corp. USA. Field Emission-Transmission Electron Microscopy (FE-TEM) and High Resolution-Transmission Electron Microscopy (HR-TEM) were assessed by JEM-2100F operated at 200 kV (JEOL, USA). FE-TEM images were obtained by spreading droplets of aqueous suspension of drug-loaded DCY51^T-AUNPS onto a carbon-coated copper grid and drying at 60°C. To acquire cross-sectioned HR-TEM images, bacterial cells containing drug-loaded DCY51^T-AuNps were initially fixed in a buffered fixative (3 % glutaraldehyde) before being deposited onto a carbon-coated grid. X-Ray Diffraction (XRD) spectra were obtained by D8 Discover with GADDS (Bruker, Germany) operating at a voltage of 40 kV and 40 mA with CuKα radiation of 1.54 Å in the 2θ range of 20-80°. Zeta potential and hydrodynamic particle size of drug-loaded DCY51^T-AUNPS suspended in distilled water were determined on a zeta potential and particle size analyzer ELS-Z2 series (Otsuka Electronics Co. Ltd., Japan) at 25°C. Pure water with a refractive index of 1.3328, viscosity of 0.8878, and dielectric constant of 78.3 was used as reference. Fourier-Transform Infrared (FTIR) spectra of CK and the corresponding drug-loaded DCY51^T-AUNPS were recorded on a PerkinElmer Spectrum 100 spectrometer. The air-dried nanoparticle powder was scanned in the range of 4000 - 450 cm^{-1} at a resolution of 4 cm^{-1} on KBr pellets.

Photoluminescence Spectra

The Photoluminescence (PL) spectra were measured at RT using the 325 nm line of a HeCd laser as the excitation source. Emitted light was collected by a lens and analyzed using a grating monochromator and a GaAs photomultiplier tube. Standard lock-in detection techniques were used to maximize the signal-to-noise ratio. The laser power for the PL excitation was about 5.66 W/cm^2.

In Vitro DPPH Radical Scavenging Activity of DCY51^T-AUNPS

In vitro antioxidant activity of DCY51^T-AuNps was evaluated using a modified method based on previous DPPH assays [17,18]. Nanoparticle solution of 20 µL was mixed with 180 µL of 1 mM methanolic DPPH solution. To obtain IC_{50}, different concentrations of AuNps (10, 100, 250, 500 µg/mL) were adopted. Gallic acid was used as positive control. The DPPH radical scavenging activity was expressed as percentage inhibition:

$$\text{DPPH radical scavenging (\%)} = \frac{A_{control} - A_{sample}}{A_{control}} \times 100\%$$

, Where A is the absorbance at 517 nm.

In Vitro Stability Study of DCY50^T-AUNPS and DCY51^T-AUNPS-CK

The stability of DCY51^T-AuNps and DCY51^T-AuNps-CK under different pH and ionic strength conditions is an important criterion for their biomedical application [19]. The intracellular pH of tumor tissues (pH 5.0–6.5) is often more acidic than physiological pH conditions of normal tissues (pH 7.4) [20]. The stability of DCY51^T-AuNps-CK in aqueous suspension was demonstrated in a wide range of pH conditions (pH2-10) by adjustment of 0.1M HCl and 0.2M NaOH at room temperature. In addition, DCY51^T-AuNps-CK was also suspended in different electrolyte conditions (10^{-1}-10^{-5} M) by addition of NaCl. No changes in the SPR peak and band as measured by UV-Vis spectrophotometer after incubation indicate the colloidal stability of nanoparticles in all of the above conditions [21].

Drug Loading Efficiency

The drug loading of DCY51^T-AuNps-CK was determined by Liquid Chromatography-Mass Spectrometry (LC-MS). The amount of CK loaded onto the nanoparticles was quantified by LC-MS. Briefly, 1 mg of air-dried drug-loaded DCY51^T-AuNps-CK was suspended in Dimethyl Sulfoxide (DMSO)-MeOH mixture (1:4, v/v). The nanoparticle suspension was sonicated overnight to ensure complete release of drug into MeOH mixture. The supernatant was collected by filtration and the amount of released drug was quantified using an LC-MS instrument [Agilent Technologies 6410 Triple Quad, chromasil C18 column (2.1 mm × 100 mm, 2.7 µm)] with distilled water (solvent A) and MeOH (solvent B) as mobile phases at 5% B and 95% A for 0 min, 60% B and 40% for 15 min, 100% B for 18 min, 100% B for 30 min,

5% B and 95% A for 32 min, and 5% B and 95% A for 32 min, all at a flow rate of 0.4 mL/min. The injection volume of each sample was 1 µL. UV detection was performed at 203 nm. Drug loading efficiency was calculated by the following formula:

Drug loading efficiency (%) =

$$\frac{\text{Total amount of drug released from nanoparticles}}{\text{Yield of nanoparticles}} \times 100\%$$

In Vitro Cell Cytotoxicity of DCY51^T-AUNPS and DCY51^T-AUNPS-CK

Cytotoxicity analysis was conducted via MTT assay in RAW264.7, HaCaT, A549, and HT29 cells according to our previous studies [14,22,23]. To investigate the cytotoxicity of drug-loaded DCY51^T-AuNps and their respective free drugs, the cells were treated with various concentrations of DCY51^T-AuNps-CK and free drug at 37°C for 48 h at 90% confluency. Finally, the absorbance of each colored solution was quantified by an Enzyme-Linked Immunosorbent Assay (ELISA) reader (Bio-Tek Instruments, Inc., Vinooski, VT, USA) at 570 nm. The optical density of formazan formed in untreated cells (negative control) represents 100% cell viability.

In Vitro Photothermal Therapy and Hoechst Nuclear Staining Assay

RAW264.7, A549, and HT29 cells were seeded onto a glass coverslips and incubated in 6-well plates at a density of 2.5×10^5 cells/mL for 24 h at 37°C in a humidified incubator with 5% CO_2 and 95% air. The cells were then incubated with a suspension of DCY51^T-AuNps or DCY51^T-AuNps-CK (1 or 5 ppm; equivalent to 0.18 and 0.89 µM of CK) for 24 h. Next, the cells were washed with 1×PBS to remove excess nanoparticles and fixed with 3.7% (v/v) formaldehyde for 5 min at room temperature. The cells were further incubated in fresh culture medium for 24 h. Subsequently, 800 nm laser (Shanghai Dream Laser Technology Co. Ltd, Shanghai, China) irradiation with a heat flux density of 0.74 W/cm^2 was applied directly above the cell plates for 10 min with a laser spot size of 0.2 cm^2, resulting in a total energy dose of 88.80 J. After irradiation, the cells were maintained at 37°C in a humidified incubator with 5% CO_2. Finally, irradiated cells were stained by Hoechst 33 258 solution (2 µg/mL) for 20 min in the dark at room temperature to analyze synergistic cell apoptosis [24]. Images of Hoechst stain were acquired by a fluorescence microscope (×400, Optinity, Korean Labtech, South Korea).

In all studies, cells without nanoparticles and cells incubated with DCY51^T -AuNps at 5 ppm served as blank and negative control and were subjected to the same irradiation conditions as cells incubated with DCY51^T-AuNps-CK. Experiments were performed in duplicates.

Total Internal Reflection Scattering (TIRS)/Differential Interference Contrast(DIC) Detection System

The schematic representation and physical layout of the apparatus were modified from previously published configurations [25]. The TIRS microscopy was carried out on an upright Olympus BX51 microscope (Olympus Optical Co., Ltd., Tokyo, Japan) equipped with a 100× oil iris objective lens (NA = 0.6-1.3, UPLANFLN, Olympus Optical Co., Ltd., Tokyo, Japan). The smallest NA value (i.e., 0.6) was used for all the experiments. TIR illumination was used: a 30-mW, 637-nm laser (MGL-III-637-200 mW, Changchun New Industries Optoelectronics Tech. Co., Ltd., China) for illumination of the gold nanoparticles. A Uniblitz mechanical shutter (model LS3S2ZO-R3, Vincent Associates, Rochester, NY, USA) and a driver (model VMM-D1, Vincent Associates) were synchronized to the Electron-Multiplying Cooled Charge-Coupled Device (EMCCD) camera (512 × 512 pixel imaging array, QuantEM 512SC, Tucson, AZ, USA). The exposure time was 100 ms. Wavelength selection was accomplished with central wavelength of 620/14 nm purchased from Semrock (Rochester, NY, USA). Lab-made DIC system was modified from previously published configurations [25]. The equipment needed for unique DIC contrast images includes a polarizer, a beam-splitting modified Wollaston prism below the condenser, a beam-recombining modified Wollaston prism above the objective, and an analyzer above polished dove prism. The illumination light was provided by a 100W halogen lamp. All images were obtained with the MetaMorph 7.5 software (Universal Imaging, Sunnyvale, CA, USA).

Statistical Analysis

All experiments were performed at least in triplicates (n=3) unless stated otherwise. Experimental data are reported as the means ± Standard Error (SEM). Statistical significances between control and sample groups were evaluated by Student's t-test with two-tailed distribution and two-sample equal variances. Greater extent of statistical significances was assigned with increasing number of asterisks (*P<0.05, **P<0.01. ***P<0.001, and ****P<0.0001).

Results and Discussion

Identification of Nanoparticle-Producing Strain

Based on 16S rRNA gene sequence analysis, the potent strain was identified as *L. kimchicus* DCY51^T (NCBI accession number EU678893, KCTC 12976^T, JSM 15530^T). *L. kimchicus* DCY51^T exhibited highest 16S rRNA gene sequence similarity with *L. odoratitofui* YIT11340^T (97.18%), *L. paracollinoides* DSM15502^T (96.97%), and *L. similis* JCM2765^T (96.93%). The same cluster was also present in the phylogenetic tree generated by maximum-parsimony algorithm (Figure S1). The genetic variation,

biochemical characteristics, and G+C mole% content (39.70 mol%) of the genomic DNA have been well characterized and previously reported by Liang et al. The morphology of the colony when grown on MRS agar at 37°C was white, circular, and convex with glossy surface and entire margin. This is consistent with the morphology previously reported [8].

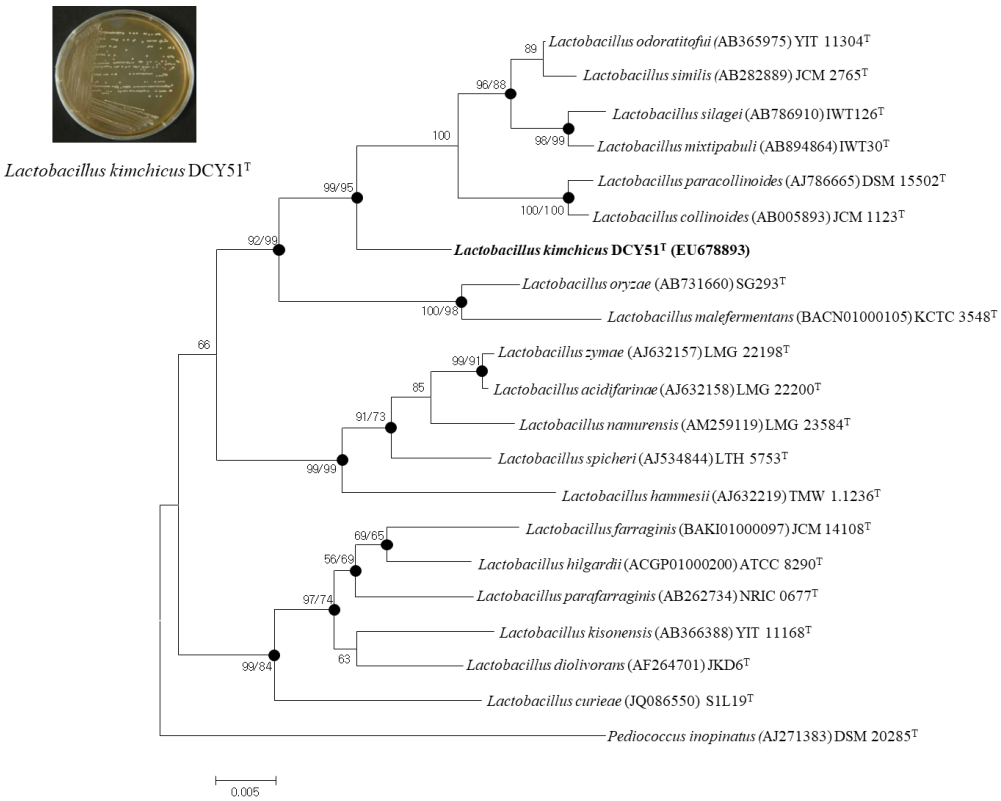

Figure S1: Neighbor-joining tree based on 16S rRNA sequences of *L. kimchicus* DCY51^T and type strains of closely related species. Inset shows colony morphology of *L. kimchicus* DCY51^T on MRS agar after 48 h of incubation at 37°C. Neighbor-joining tree based on 16S rRNA gene sequence analysis showing phylogenetic relationship of strain *L. kimchicus* DCY51^T and members of the genus *Lactobacillus*. Filled circles indicate that the corresponding nodes were also recovered in the maximum-parsimony tree. Bootstrap values (>50%) based on 1000 replications are shown at branching points. *Pediococcus inopinatus (*AJ271383) DSM 20285^T was used as an out group. Scale bar, 0.005 substitutions per nucleotide position.

One-Pot biosynthesis of DCY51^T-AuNps and DCY51^T-AUNPS-CK

Whole cells of *L. kimchicus* DCY51^T were used as biocatalysts in nanoparticle synthesis (Figure 1). Although utilizing intracellular enzyme may potentially eliminate the downstream process of purifying nanoparticles, it requires coenzymes (i.e. NADH, NADPH, FAD, etc.) to sustain bioreduction [26-28]. While considering the scalability potential of the process, the use of whole cells is favored because coenzymes are recovered during the metabolic pathways in live whole cells and thus, the replenishment of expensive coenzymes is avoided [26,28]. Moreover, Nair and Pradeep reported that small nanoclusters observed outside of the bacterium had the tendency to aggregate [29]. In other words, nanoparticles produced by intracellular enzymes or cell extract were less stable than those synthesized inside the cells [26,27].

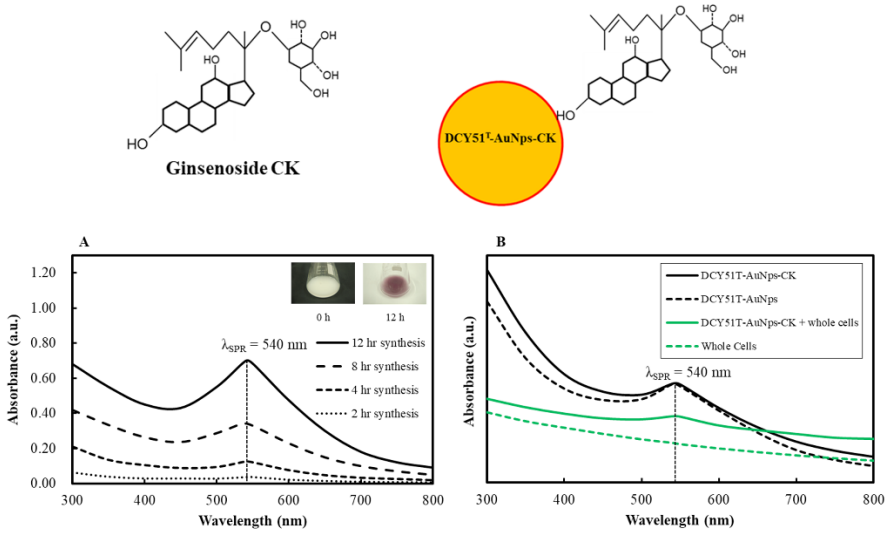

Figures 1(A, B): UV-Vis absorbance spectra of DCY51^T-AuNps and DCY51^T-AuNps-CK. DCY51^T-AuNps **(A)** and DCY51^T-AuNps-CK **(B)**. Insets from **(A)** showed color change of cell biomass due to SPR of DCY51^T-AuNps present in the reaction mixture. The peak at ~540 nm corresponds to the surface plasmons in the AuNps. The peak intensity increased with time due to the oxidation of protein by gold ions. There is no change in the SPR peak between DCY51^T-AuNps and DCY51^T-AuNps-CK after 12 h of incubation, meaning that there is no significant change in the shape, surface, and agglomeration state between the two nanoparticles. For comparison, in **(B)**, we display the absorption of whole cells and a sample where nanoparticles were growing within or on the surface of bacterial cells.

The synthesis of DCY51^T-AuNps and DCY51^T-AuNps-CK was screened by visual observation through a color change in the reaction mixture. Prior to incubation, the color of the reaction mixture consisting of biomass suspended in distilled water was yellowish-white. After the addition of 1 mM of gold salt, the color of the cell biomass consequently shifted to deep purple (Figure 1A). No further color change was observed after 12 h of incubation. After 24 h, the purple biomass settled to the bottom of the flask, leaving a clear and colorless supernatant in the mixture. The growth medium alone as well as the growth medium after removal of cell biomass did not exhibit any color changes when incubated with gold salts. These observations indicated that DCY51^T-AuNps and DCY51^T-AuNps-CK were synthesized intracellularly or on the cell surface. To isolate the biosynthesized colloidal gold from microbial cells, cell biomasses containing nanoparticles were harvested by centrifugation and subjected to several cycles ultra-sonication to thoroughly disrupt the cells.

The rise to the sharp and intense purple color of the cell biomass is the response of SPR phenomena of AuNps: the light ray which diffuses around the colloidal nanoparticles excites the free electrons, resulting in oscillations that reverberate with the frequency of visible light wavelengths [10,11,30]. Even though the exact mechanism of green synthesis has not yet been thoroughly elucidated, many reports have shed some light on the intracellular synthesis of AuNps by *Lactobacillus* species [26,29,31]. It has been postulated that sugars and NADH-dependent enzymes secreted by the microorganism on the cell surface are responsible for the reduction of gold ions while proteins (or peptides) and amino acid residues inside the cells are responsible for providing stabilization of nanoparticles [26,31,32]. The positively-charged metal ions are attracted to the negatively-charged cell wall from the carboxylate groups via electrostatic interaction. The metal nuclei are then transported into the microbial cells due to these interactions where they aggregate to form larger sized particles through further reduction and aggregation [29,32].

Several non-covalent interactions, including electrostatic interactions, hydrogen bonds, hydrophobic forces and van der Waals forces, are conjectured to play key roles in the binding process of proteins with ginsenoside CK to the surface of DCY51^T-AuNps [33]. Furthermore, poorly water soluble ginsenoside CK may also move into the hydrophobic micro-regions of the proteins stabilizing the nanoparticles [34].

UV-Vis spectra analysis of DCY51^T-AuNps and DCY51^T-AUNPS-CK

UV-Vis spectroscopy analysis was used to monitor the visible absorption bands of nanoparticles. These absorption bands are strongly dependent on the nanoparticle size, shape, surface, and agglomeration state [15,35]. Nanoparticles with larger crystallite sizes or particle agglomeration often have broad absorption bands

spanning into the red-shifted range (>600 nm) due to the presence of both transversal and longitudinal SPRs [36].

The time-dependent extinction spectra of DCY51^T-AuNps showed a major absorbance peak measured at ~540 nm (λ_{SPR}). The absorbance peaks can be attributed to the SPR band of gold [10,11]. The optimal absorbance value was obtained during 12 h incubation. No higher absorbance peak was observed in UV-Vis spectrum recorded after 24 h. Likewise, the extinction spectra of DCY51^T-AuNps-CK exhibited a major absorbance peak at ~540 nm after 12 h of incubation at 37°C (Figure 1B). There is no change in the SPR peak between drug-loaded nanoparticles and DCY51^T-AuNps, meaning that there is no significant change in the size, shape, surface, and agglomeration state between the two nanoparticles. The sharpness of SPR peaks of DCY51^T-AuNps and DCY51^T-AuNps-CK revealed that the biosynthesized nanoparticles were suitable for better sensing resolution as bio-imaging tags in dark-field microscopy techniques [30]. For comparison, we display the absorption of whole cells and a sample where nanoparticles were continuously reduced within or on the surface of bacterial cells: as expected, whole cells of *L. kimchicus* DCY51^T did not contribute to the peaks observed in DCY51^T-AuNps and DCY51^T-AuNps-CK.

TEM analysis of DCY51^T-AuNps and DCY51^T-AUNPS-CK

AuNps were further analyzed by FE-TEM and HR-TEM. FE-TEM images showed spherical DCY51^T-AuNps and DCY51^T-AuNps-CK with varying sizes of 5–30 nm (Figure 2B, C). Subsequently, FE-TEM and HR-TEM analysis after 12 h of incubation exposed the presence of gold nanoclusters within the bacteria (Figure 2A, F). Figure 2A revealed that the spherical DCY51^T-AuNps were found exclusively inside the cell envelope or cell membrane. From FE-TEM results, it is evident that after cell rupture and purification, the synthesized DCY51^T-AuNps retained their shapes. This observation suggests that nanoparticle synthesis was localized within bacterial cell envelope or cell membrane. Upon further investigation by cross-sectional HR-TEM (Figure 2F), DCY51^T-AuNps-CK were more concentrated upon the bacterial capsule and cell wall than on the cytoplasmic membrane, possibly due to reduction of the metal ions by enzymes and exopolysaccharides present in the cell wall and slime layer. Few of the nanoparticles were found to be transported into the cytoplasmic membrane where they further aggregated.

Elemental mapping showed the distribution of elemental gold in the isolated DCY51^T-AuNps (Figure 2C, D) and DCY51^T-AuNps-CK (Figure 2H, I). The distribution of gold was clearly visible in the electron image and was found to be the predominant element in the nanoparticles (Figure 2D, I). Energy-Dispersive X-Ray spectroscopy (EDX) analysis of DCY51^T-AuNps (Figure 2K) and DCY51^T-AuNps-CK (Figure 2L) demonstrated the highest optical absorbance band peaks at 2.3 keV, which corresponded to the characteristic peak of metallic gold [37].

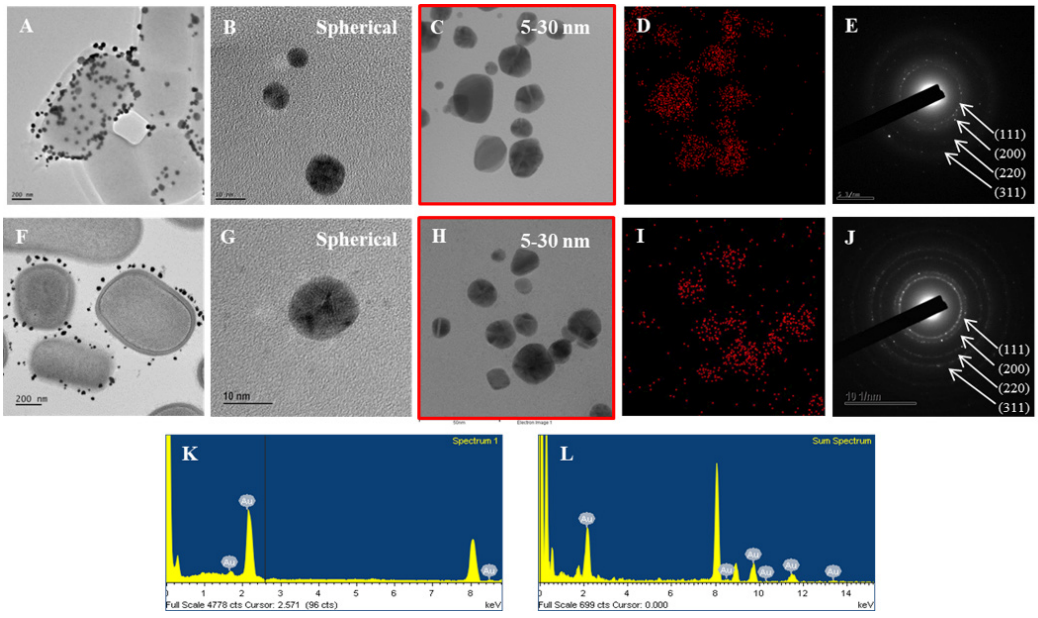

Figures 2(A-L) TEM analysis of DCY51^T-AuNps and DCY51^T-AuNps-CK. TEM images of DCY51^T-AuNps **(A, B)** and DCY51^T-AuNps-CK **(F, G)**. Gold distribution of DCY51^T-AuNps **(C, D)** and DCY51^T-AuNps-CK **(H, I)**. SAED of DCY51^T-AuNps **(E)** and DCY51^T-AuNps-CK. EDX of **(J)** DCY51^T-AuNps **(K)** and DCY51^T-AuNps-CK **(L)**.

XRD Profile and Photoluminescence (PL) Spectroscopy Analysis of DCY51^T-AUNPS-CK

The crystalline nature of the biologically synthesized nanoparticles was evaluated by XRD analysis. Figure 3A demonstrated the intensive diffraction patterns of biosynthesized DCY51^T-AuNps and DCY51^T-AUNPS-CK. The four characteristic peaks of gold were indexed to (111), (200), (220), and (311) lattice plane of Bragg's reflection. The intensities measured at (200), (220), and (311) lattice planes were much lower than (111) plane, which suggests that the nanoparticles were primarily composed of (111). The average diameters of DCY51^T-AuNps and CK-loaded DCY51^T-AuNps were estimated by taking the Full Width at Half Maximum (FWHM) of the most intense diffraction peak [(111) lattice plane] and Debye-Scherrer equation; the resulting nanoparticles maintained an average crystallite size of ~13.26 nm and ~6.04 nm, respectively. Ginsenoside loading results in smaller nanoparticles probably due to supplementary reduction and stabilization of gold atoms by self-assembled monolayer of ginsenoside CK, curtailing nanoparticle growth by aggregation.

Particle Size Distribution of DCY51^T-AUNPS and DCY51^T-AUNPS-CK

The size distribution profile of AuNps was performed by particle size analyzer according to intensity (Figure 3B, C). Size distribution histogram of DCY51^T-AuNps (Figure 3B) unveiled a wide range of particle size distribution varying from 40–300 nm with a Z-average value of 130.20 ± 2.05 nm and a PDI of 0.28 ± 0.01. According to FE-TEM images (Figure 3B-C) and DLS analysis, DCY51^T-AuNps synthesized by *L. kimchicus* DCY51^T were not entirely monodisperse: the nanoparticles were, in fact, moderately poly-disperse: a common distribution type typically resulted from biological synthesis [10,11]. The discrepancy in the nanoparticle sizes analyzed by XRD (and FE-TEM) and DLS is attributed to the fact that XRD (and FE-TEM) anticipates the crystallite size of nanoparticles in dried form whereas DLS measures the hydrodynamic size of nanoparticles in aqueous suspension, which includes the metallic core and any biological molecules attached or adsorbed on the particle surface [30]. Similarly, the hydrodynamic diameter of DCY51^T-AuNps-CK was 134.25 ± 1.15 nm and a PDI of 0.13 ± 0.00 (Figure 3C).

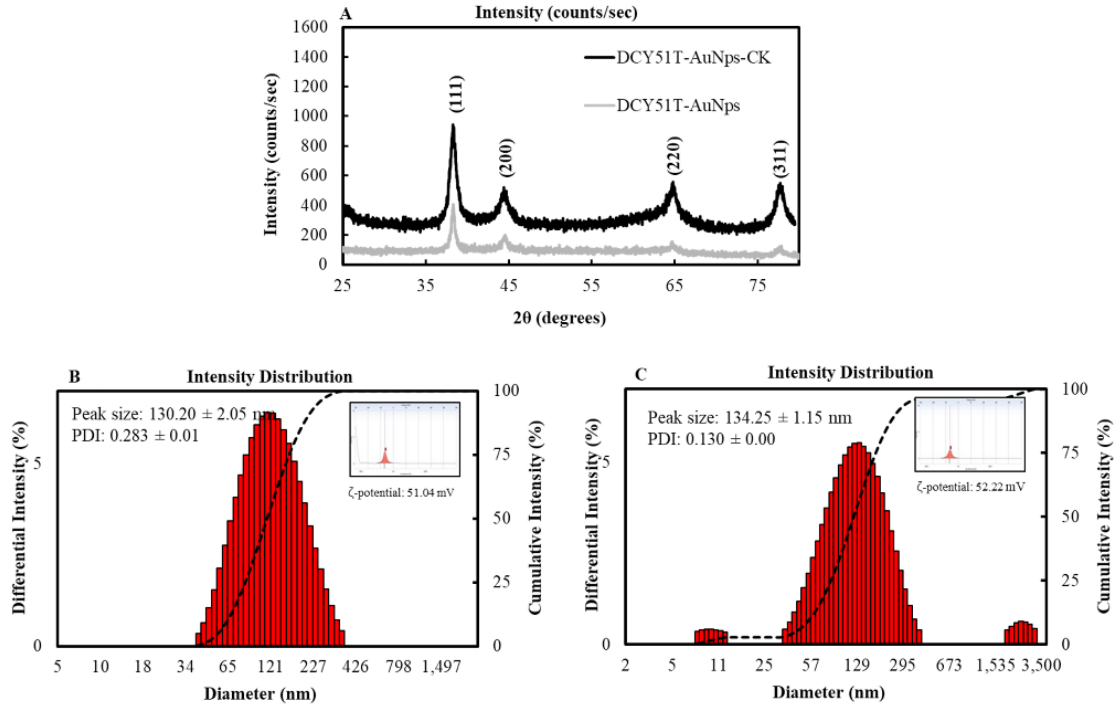

Figures 3(A-C): XRD patterns and Particle size distribution of the obtained nanoparticles. XRD patterns of DCY51^T-AuNps and DCY51^T-AuNps-CK **(A)**. DCY51^T-AuNps **(A)** and DCY51^T-AuNps-CK **(B)**. Insets demonstrate the zeta potential of DCY51^T-AuNps **(A)** and DCY51^T-AuNps-CK **(B)**.

During the formulation of DCY51^{T}-AuNps-CK, the hydrodynamic diameter size was increased up to ~4 nm. This result indicated the successful loading of ginsenoside CK onto the surface of DCY51^{T}-AuNps [38]. However, large micron-sized particles suspected to be aggregated nanoparticles or dust were observed Figure 4A-B; these larger particles might skew the PDI value to a lower magnitude due to the masking of scattering intensity of small particles by large aggregates [39]. Additionally, light scattering analysis also discovered small particles below <20 nm.

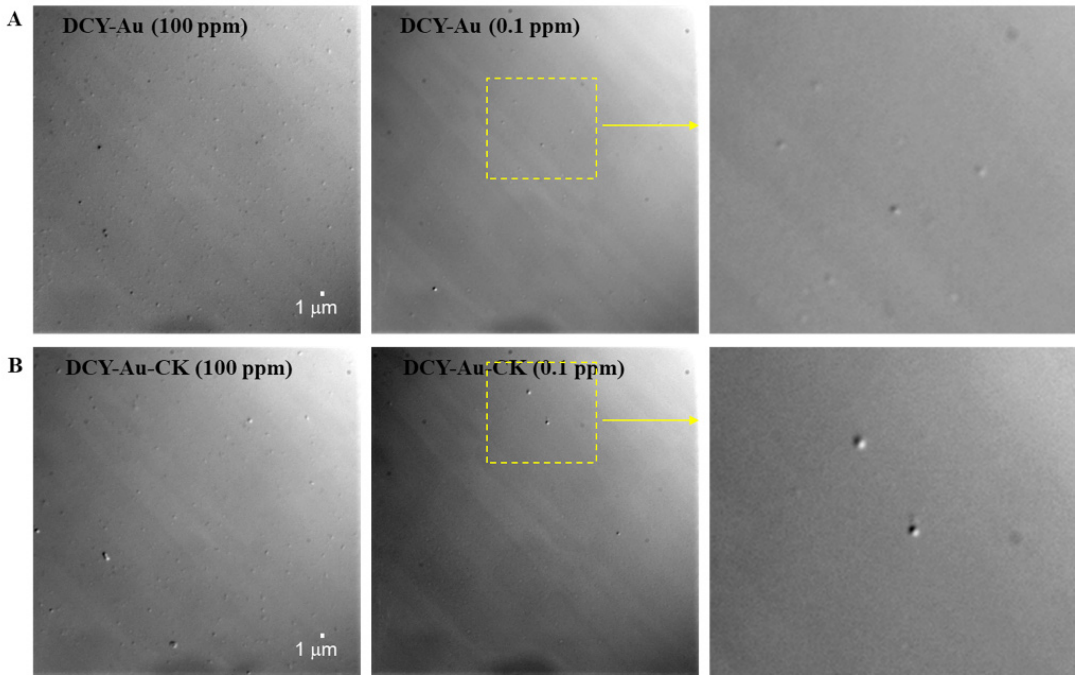

Figures 4(A, B): Total Internal Reflection Scattering (TIRS)/Differential Interference Contrast (DIC) detection system. **A**. DCY-Au; **B**. DCY-Au-CK.

These particles could be due to the released ginsenoside CK in the suspension which then were expected to form insoluble "Clumps" in aqueous medium (Figure 5A-B). The Photoluminescence (PL) spectroscopy was performed. Intensity of DCY51^{T}-AuNps-CKs was shown at 425nm (Figure 5C).

At neutral pH in distilled water, the zeta potentials (ζ) of DCY51^{T}-AuNps and DCY51^{T}-AuNps-CK were determined to be ~51.04 mV and ~52.22 mV, respectively, implying the stable nanoformulations in the aqueous suspension. The small increase in the positive charge indicated that other attractive forces, such as van der Waals forces or hydrogen bonding, might be responsible for facilitating the drug loading process [19]. According to previous studies, nanoparticles of ≤200 nm may accumulate in tumor tissues due to the enlarged gap junctions (100 nm-2 µm) in the poorly aligned and defective endothelia lining. This Enhanced Permeability and Retention (EPR) effect is the main mechanism of non-targeted drug delivery system [40]. Furthermore, the cationic charge of DCY51^{T}-AuNps-CK may induce higher cellular uptake and greater cytotoxicity to cancer cells due to their permeability to the anionic cell membrane [41].

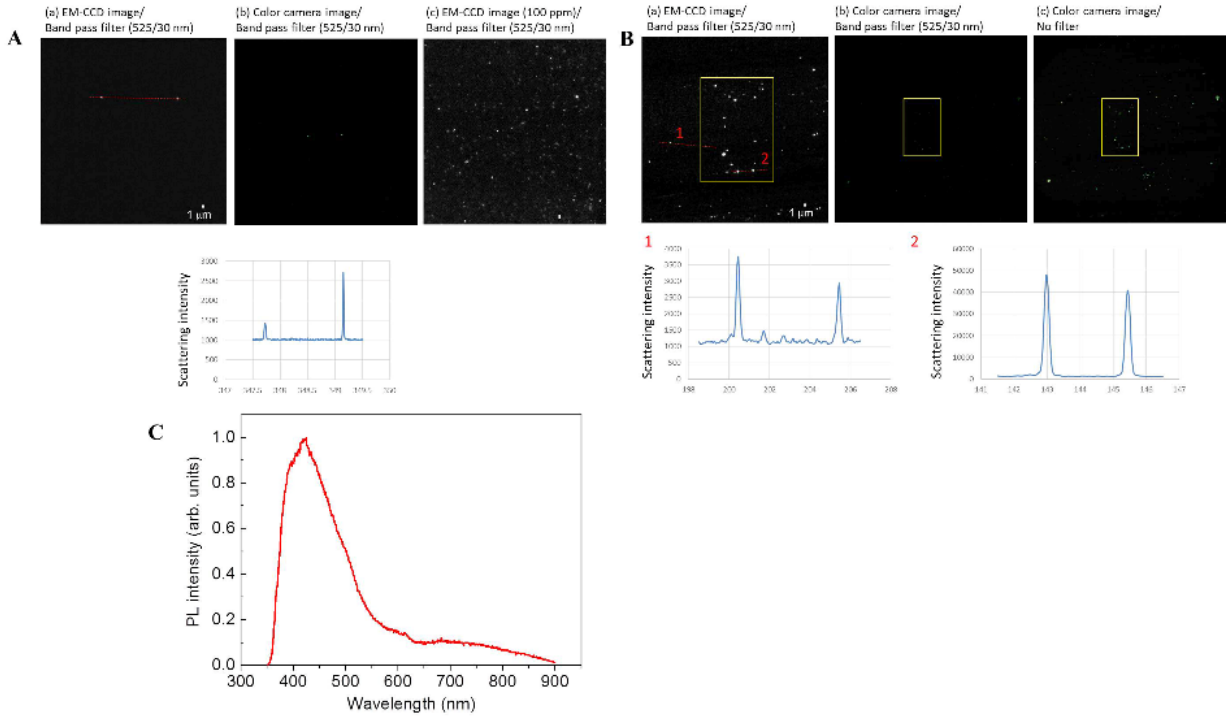

Figures 5(A-C): Enhanced Dark Field Image: **A**. DCY51^T-Au (0.1 ppm in water); **B**. DCY51^T-Au-CK (0.1 ppm in water); **C**. Photoluminescence of DCY51^T-Au-CK.

FTIR Profile Analysis of DCY51^T-AuNps and DCY51^T-AUNPS-CK

FTIR spectrum of DCY51^T-AuNps-CK was compared against ginsenoside CK, DCY51^T-AuNps. *L. kimchicus* DCY51^T, and gold salt (Figure S2). It is evident that the biosynthesized DCY51^T-AUNPS possessed additional bands that were not originally observed in the gold salt. The bands shown at 3422.71, 2935, 1233.92, 1048.49 cm^{-1} are due to the stretching vibrations of hydroxyl (O-H) or primary amines (N-H), alkane (C-H), amine (C-N), and alcohol (C-O) groups, respectively [17,42]. Bending vibration of alkane groups (C-H) was observed at 1378 cm^{-1}. Amide bands containing carbonyl groups (C=O) were observed at 1648 cm^{-1}[43]. These bands correspond to the carbonyl stretching in the amide linkages of the protein residues [17]. Proteins and amino acid residues (e.g. cysteine, tyrosine, and tryptophan) are reported to be responsible for providing stability to bacteria-mediated AuNps [14]. Few studies have reported that AuNps have characteristic binding affinity to thiols, amines, and amides, which are present in amino acid residues [44]. Proteins or peptides can also bind to DCY51^T-AuNps via electrostatic interaction from the negatively-charged carboxylate groups found in NADH-dependent enzymes secreted on the cell wall [45]. Strong characteristic peaks of primary amines and carbonyl stretch in the amide linkages suggest that free amino groups due to amino acid residues and surface-bound proteins are culpable for the formation of protein capping layers on the nanoparticles and preventing their agglomeration [31].

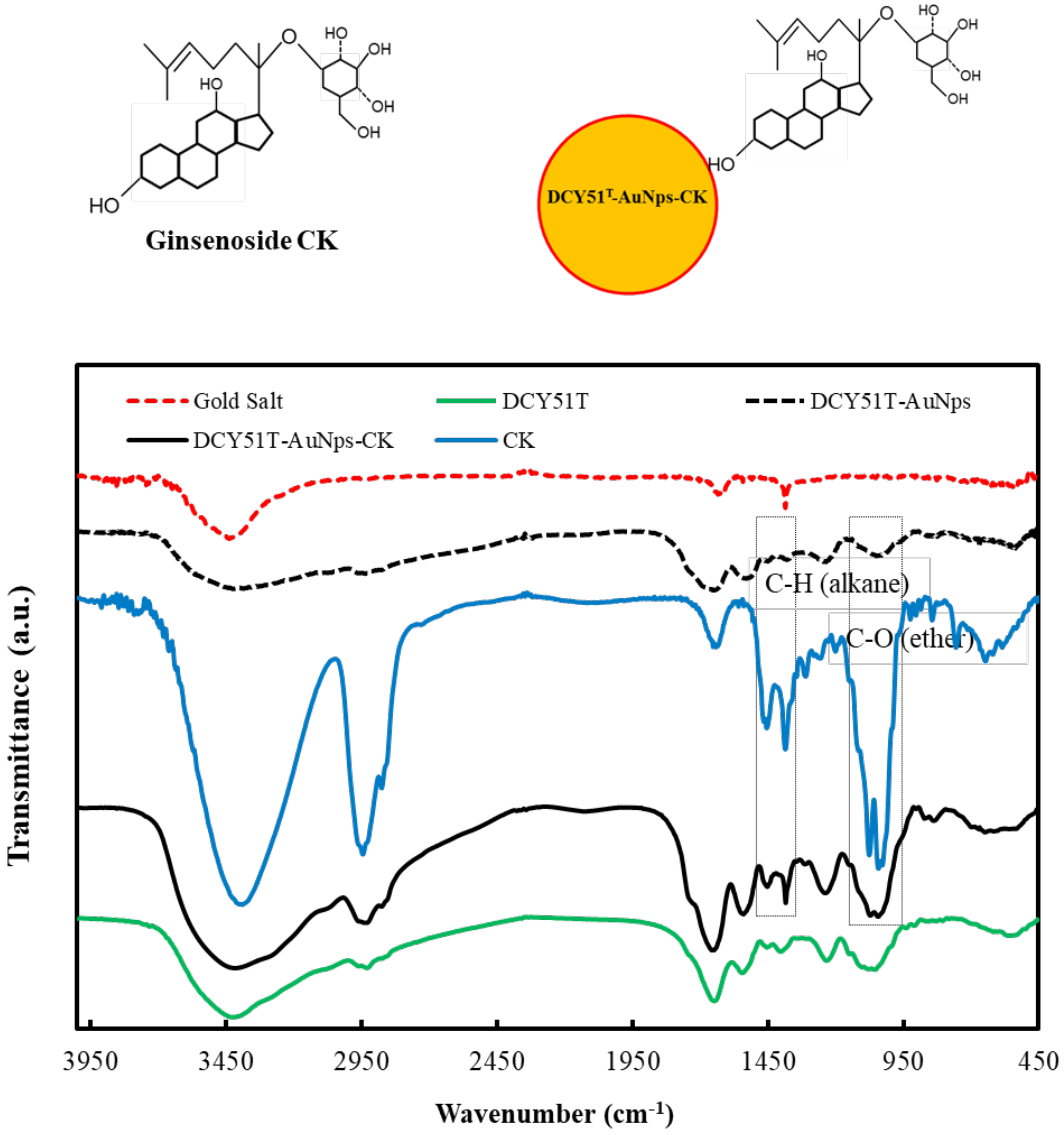

Figure S2: FTIR spectra of DCY51^T-AuNps and DCY51^T-AuNps-CK and proposed ginsenoside CK complexation onto the surface of DCY51^T-AuNps. Gold salt (red, dashed line), whole cells of *L. kimchicus* DCY51^T (green, solid line). DCY51^T-AuNps (black, dashed line), DCY51^T-AuNps-CK (black, solid line), and ginsenoside CK (blue, solid line). FTIR spectra of DCY51^T-AuNps-CK revealed the presence of C-H bends (alkane groups) and C-O stretch (ethers) of ginsenoside CK.

The complexion of ginsenoside CK with DCY51^T-AuNps-Ck is confirmed by the bands observed in the wavenumbers corresponding to the alkanes (C-H) and ethers (C-O) of ginsenoside CK observed from 1500-1440 cm^{-1} and 1300-1000 cm^{-1}, respectively [46]. These peaks were suspected to be the result of the non-covalent attractive forces between ginsenoside CK and DCY51^T-AuNps: after nucleation and stabilization by surface-bound proteins, ginsenoside CK might form stable, non-covalent interactions with the positively-charged amino groups on the surface of DCY51^T-AuNps. In addition, the hydroxyl group in the C_3 position of ginsenoside CK was hypothesized to be vulnerable to losing electrons and thus, it might act as the reducing species for the reduction of Au^{3+} ions into Au^0 and oxidize into carboxylic acid [46,47].

In Vitro DPPH Radical Scavenging Activity of DCY51^T-AuNps

The antioxidant activity of DCY51^T-AuNps was evaluated *in vitro* according to previous methods with slight modifications [17,18]. DPPH reducing ability of DCY51^T-AuNps was assessed colorimetrically from purple to yellow at 517 nm. DPPH is composed of stable free radical molecules and is readily reduced by accepting hydrogen or electron from nanoparticles [18]. Figure S7 revealed that the biologically synthesized DCY51^T-AuNps possessed free radical scavenging activity. The scavenging activities increased in a dose-dependent manner and were significantly higher than those exhibited by their precursor salts. The recorded percentage scavenging ability for the lowest concentration of the biosynthesized DCY51^T-AUNPS (10 µg/mL) was 18.17 ± 2.34 and this scavenging ability was increased to 60 ± 1.82 when concentration was increased to 500 µg/mL.

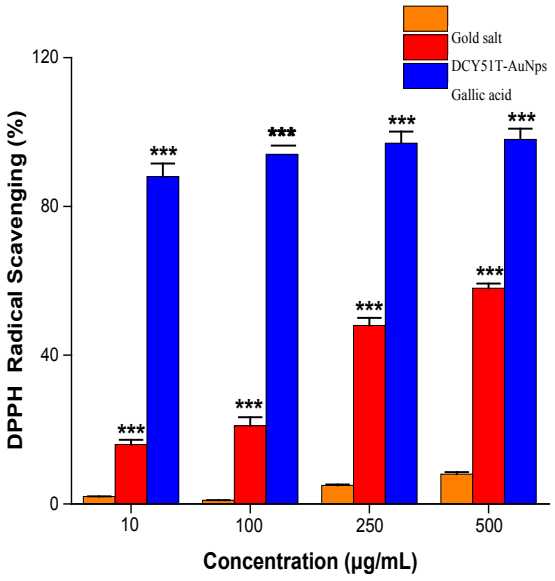

Figure S7: Dose-dependent *in vitro* DPPH radical scavenging activity of DCY51^T-AuNps. Gold salt (orange), DCY51^T-AuNps (red), and gallic acid (blue).

The increased free radical scavenging activity of biosynthesized DCY51^T-AuNps can be attributed to the antioxidant activity of probiotic *L. kimchicus* DCY51^T [18]. This result evidently suggests that the protective capping of DCY51^T-AuNps by various amino acid residues and surface-bound proteins seems to be the major contributors to the increased free radical scavenging activity. The IC_{50} value was calculated graphically and determined to be 0.25 ± 0.01 mg/mL. Numerous studies have been carried out on the synthesis, characterization, and antimicrobial activites of silver nanoparticles by *Lactobacillus* spp. However no report is available on the biomedical application of AuNps by *Lactobacillus* spp. Thus, we aimed to study the capability of *L. kimchicus* DCY51^T-mediated intracellular synthesis of DCY51^T-AuNps as novel antioxidant agents. In this study, we report that the biosynthesized AuNps possess higher antioxidant activity as compared to gold salt and demonstrate potentials as free radical scavengers, preventing these radicals from causing cell or DNA damage which may take part in the development of cancer and other health conditions [48].

In Vitro Stability Study of DCY51^T-AuNps and DCY51^T-AuNps-CK

Stability of drug-loaded nanoparticles is an essential requirement for their therapeutic and biomedical application [19]. Nanoparticles must be impervious to aggregation induced by pH variation or a high ionic strength environment, mocking the interactions of nanoparticles with biological interfaces in physiological conditions. AuNps obtained by chemical reduction aggregate at the slightest alteration in their pH and/or electrolytic environments [21]. This feature was analyzed by monitoring the SPR of nanoparticles by UV-Vis spectroscopy at 200 µg/mL in aqueous suspensions under different pH and electrolytic conditions over a reasonable period of time at room temperature. The surface plasmon wavelength (λ_{SPR}) shift to a larger value and/or the excessive broadening of the absorption band can be attributed to the increased crystallite size of the nanoparticles or particle aggregation or both which decreases the sensitivity to plamon response [30]. There was no bathochromic shift in the surface plasmon wavelength at ~540 nm and minimal change (<0.1) in the absorbance values against varied pH conditions (2-10) and the concentration of electrolyte (NaCl) up to 10^{-1} M (Figure 6A-B). The *L. kimchicus* DCY51^T-stabilized nanoparticles were stable for at least three months at 4˚C (Figure 6C). These results confirmed the colloidal stability of DCY51^T-AuNps and DCY51^T-AuNps-CK by *L. kimchicus* DCY51^T in all of the above experimental conditions. To boot, the colloidal stability of DCY51^T-AuNps and DCY51^T-AuNps-CK in aqueous medium was substantiated by the relatively high ζ-potential high magnitude of ζ-potential indicates that the nanoparticles will resist aggregation resulted by electrostatic repulsion between nanoscale particles [49].

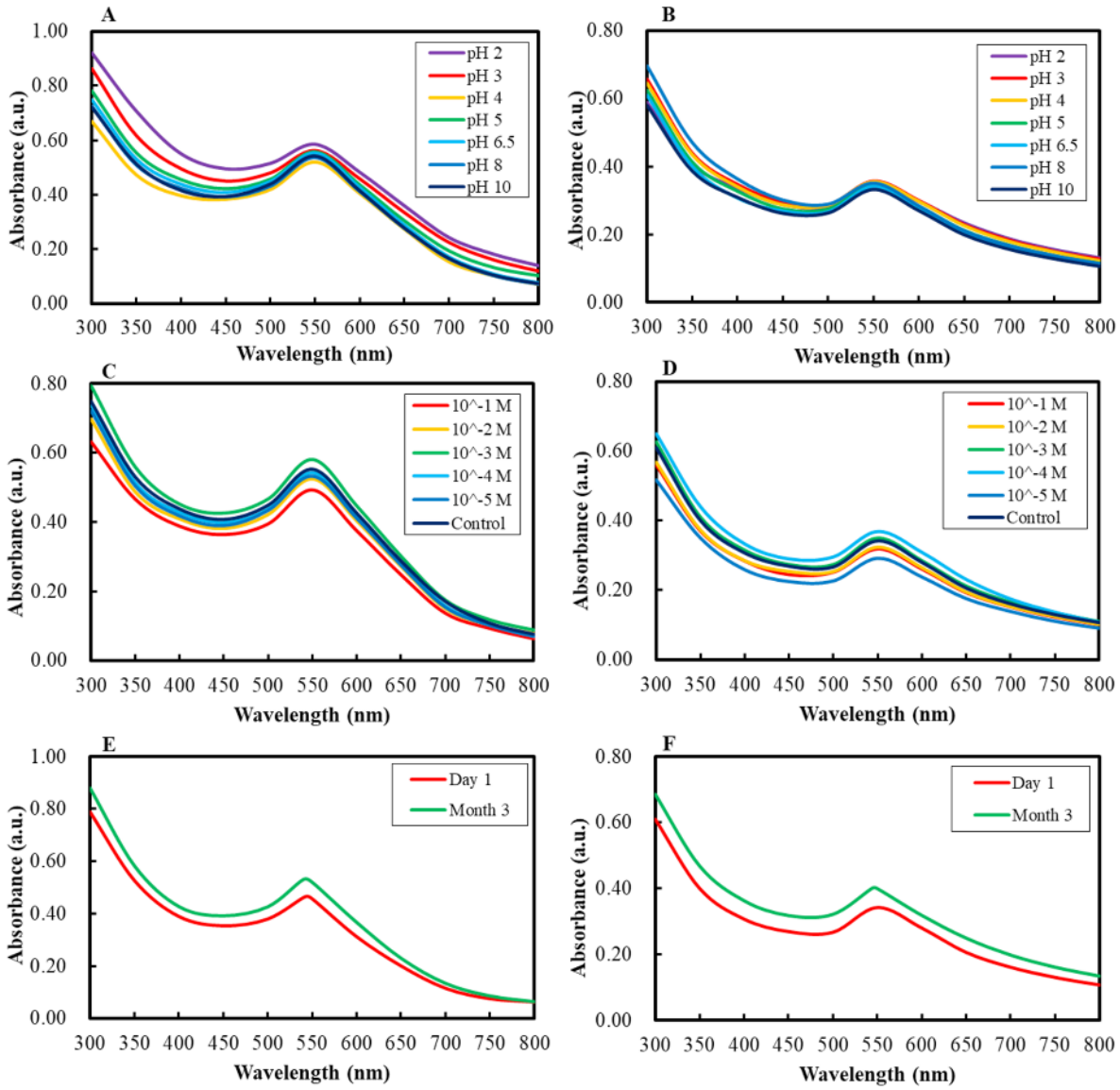
A
Absorbance (a.u.)
Wavelength (nm)
pH 2
pH 3
pH 4
pH 5
pH 6.5
pH 8
pH 10
B
Absorbance (a.u.)
Wavelength (nm)
pH 2
pH 3
pH 4
pH 5
pH 6.5
pH 8
pH 10
C
Absorbance (a.u.)
Wavelength (nm)
10^-1 M
10^-2 M
10^-3 M
10^-4 M
10^-5 M
Control
D
Absorbance (a.u.)
Wavelength (nm)
10^-1 M
10^-2 M
10^-3 M
10^-4 M
10^-5 M
Control
E
Absorbance (a.u.)
Wavelength (nm)
Day 1
Month 3
F
Absorbance (a.u.)
Wavelength (nm)
Day 1
Month 3

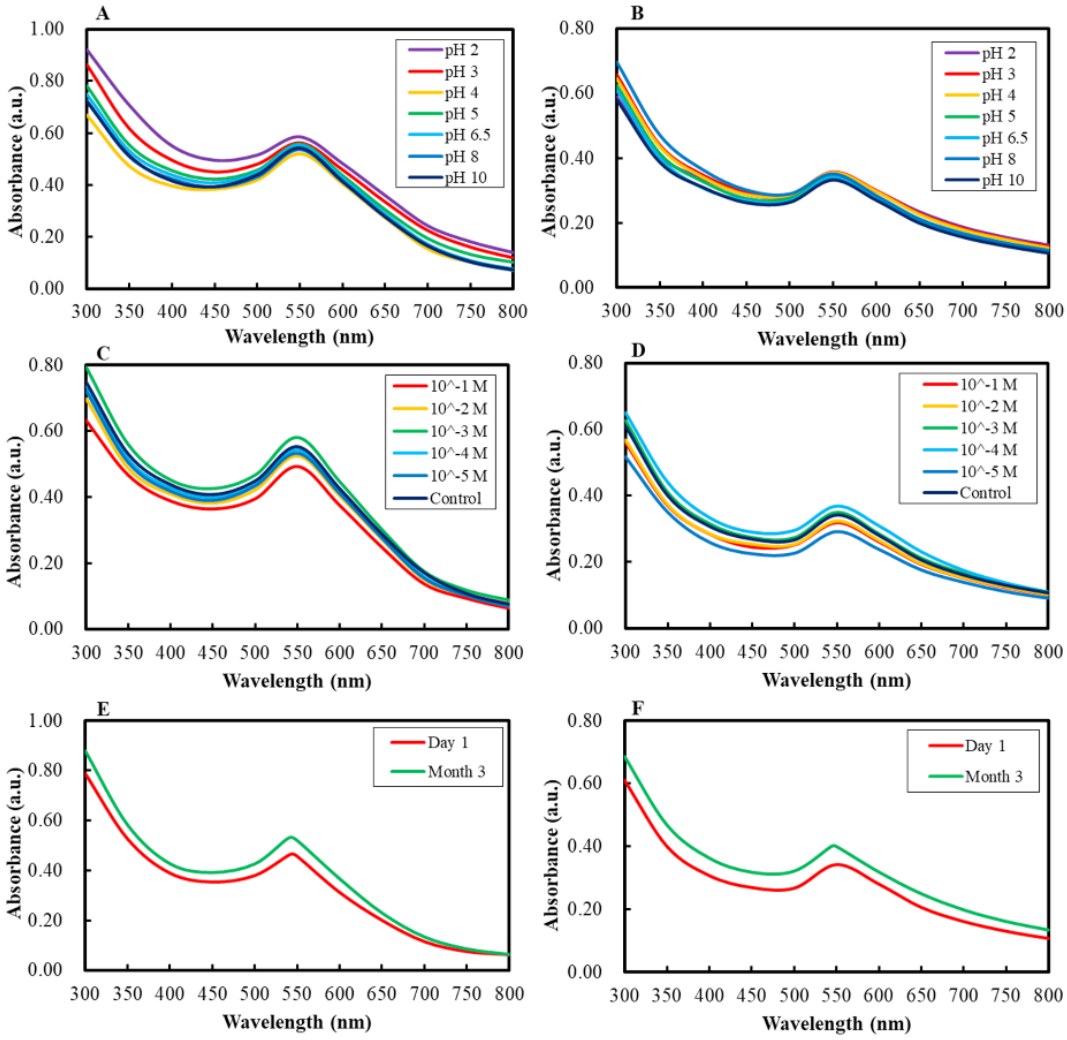

Figures 6(A-F): UV-Vis absorbance spectra of DCY51^{T}-AuNps and DCY51^{T}-AuNps-CK nanoparticles depicting their high stability in various conditions. Stability of these nanoparticles against varied pH conditions **(A, B)** and electrolytic concentrations **(C,D)**, respectively. Three-month stability showing no aggregation. DCY51^{T}-AuNps **(E)** and DCY51^{T}-AuNps-CK **(F)**.

Drug Loading Efficiency

Quantification of the concentration of ginsenoside CK in the drug-loaded DCY51^{T}-AuNps is a critical parameter to evaluate the properties of the nanoformulation. CK-loaded DCY51^{T}-AuNps were exposed to DMSO-MeOH mixture (1:4, v/v) and sonication at room temperature for 24 h to allow complete release of CK and evaluation of the drug loading efficiency. The majority of the released drug was expected to be separated in the MeOH fraction since the loaded drug has high solubility in MeOH [50]. As shown in Figure S3, the peak of ginsenoside CK was also detected in the intracellular content of bacterial debris and supernatant after purification of DCY51^{T}-AuNps-CK, indicating that the encapsulation efficiency of ginsenoside CK is well beneath 100%. At the end of 24 h, approximately 110.30 µg of ginsenoside CK per one mg of DCY51^{T}-AuNps-CK was released in the medium. Calibration curve was prepared by standard CK with known concentrations in the range of 10-100 µg/mL (regression equation: $y = 1{,}203{,}623.2951x + 8{,}433{,}298.2623$; $R^2 = 99.86\%$). Thus, the drug loading efficiency is determined to be ~11.03%.

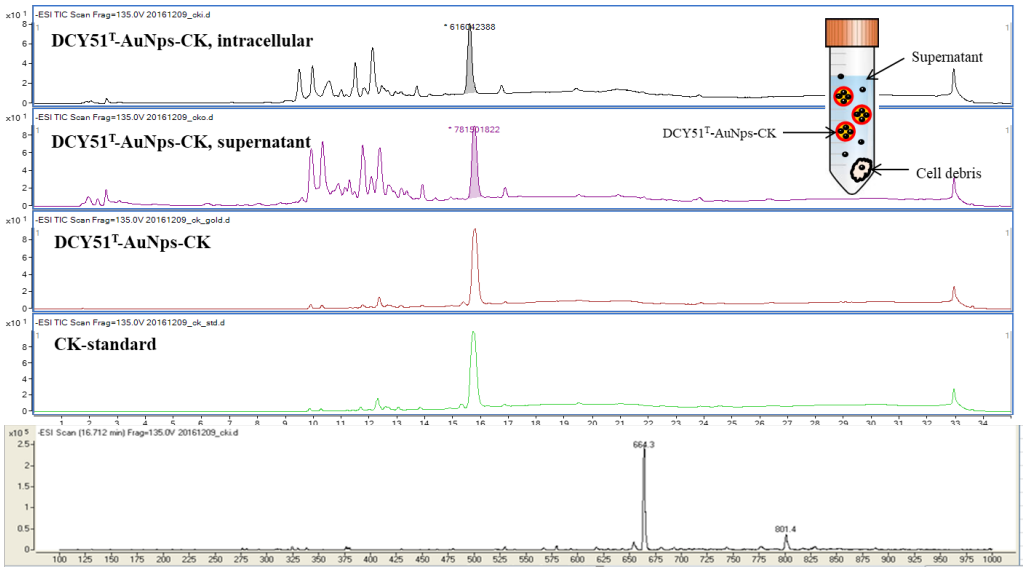

Figure S3: LC-MS spectra of ginsenoside CK released from DCY51^T-AuNps-CK after 24 h of sonication in DMSO-MeOH mixture (1:4, v/v). Inset distinguishes the ginsenoside CK released from the intracellular content of cell debris, supernatant, and purified DCY51^T-AuNps-CK.

The released CK from DCY51^T-AuNps-CK was subjected to mass spectroscopy to determine its molecular weight. The molecular weight of the ginsenoside obtained from DCY51^T-AuNps-CK was determined to be 618.3 which is similar to the molecular weight of CK (622.88) (Mass spectrum of CK, m/z = 664.3 = [MW + formic acid], MW 618.3)

In Vitro Cell Cytotoxicity of DCY51^T-AuNps and DCY51^T-AuNps-CK

The cytotoxicity of DCY51^T-AuNps, DCY51^T-AuNps-CK, and ginsenoside CK was evaluated in normal (RAW264.7 and HaCaT) and cancer (A549 and HT29) cell lines via MTT assay. Colorimetric assessment of cell viability was measured using the ELISA reader after 48 h of incubation. The results of MTT assay for DCY51^T-AuNps are shown in Figure S4. Upon close observation, the viability of the cells bounced back as the concentration of DCY51^T-AuNps was increased to 100 µg/mL in murine macrophage (93.33 ± 0.97%), human keratinocyte (81.42 ± 3.76%), and lung adenocarcinoma cells (74.24 ± 1.16%).

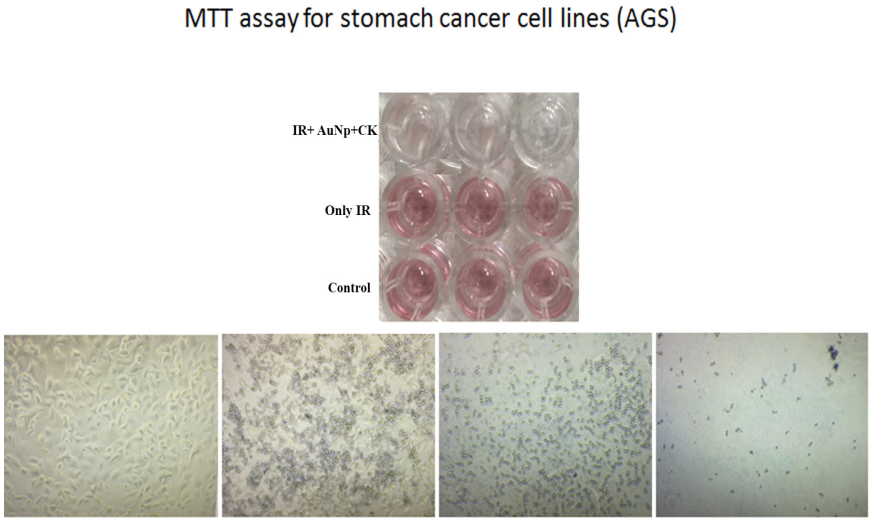

Figure S4: Anticancer activity of the AuCkNPs on the stomach cancer cell lines (AGS).

On the other hand, colon adenocarcinoma cells showed a dose-dependent cell inhibition as the concentration of DCY51^T-AuNps was increased from 1-100 µg/mL (81.90 ± 1.16% to 57.67 ± 2.65%) (Figure S5). Moreover, DCY51^T-AuNps started to exhibit significant cell inhibition at 1 µg/mL in murine macrophage, human keratinocyte, and adenocarcinoma cells ($P<0.05$). However, cell inhibition was significantly reduced starting at 0.01 µg/mL in lung adenocarcinoma cells ($P<0.01$). Thus, DCY51^T-AuNps served as suitable delivery agents for ginsenoside CK in cancer cells.

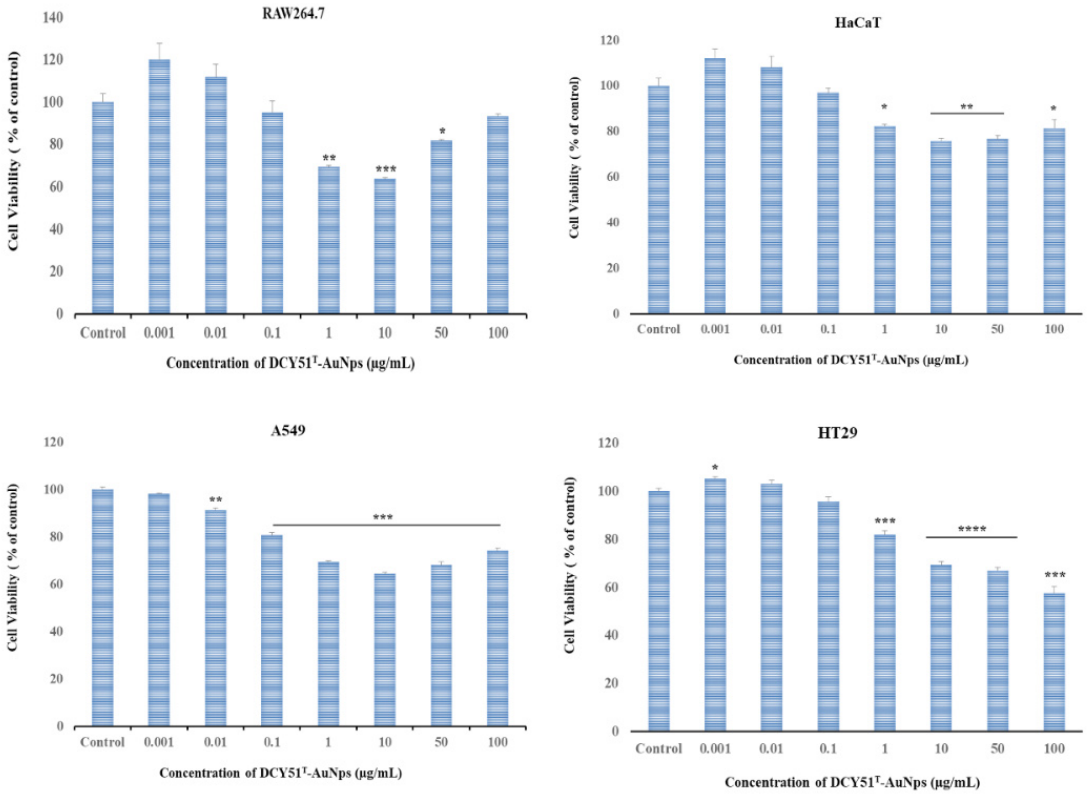

Figure S5: Cytotoxicity of DCY51^T-AuNps after 48 h of incubation. RAW264.7 **(A)**, HaCaT **(B)**, A549 **(C)**, and HT29 **(D)** cells.

Similarly, the cytotoxicity of DCY51^T-AuNps-CK and standard ginsenoside CK was evaluated in normal (RAW264.7) and cancer (A549 and HT29) cell lines via MTT assay. The results are shown in Figure 7A-C. Sufficient concentrations of DCY51^T-AuNps-CK were used such that the concentration of CK in the free drug was comparable to that in the drug-loaded nanoparticles. Based on MTT results, DCY51^T-AuNps-CK were found to exert less cytotoxicity compared to free CK in murine macrophage and human keratinocyte cell lines (Figure 7A-C). At 20 µM of equivalent CK content, DCY51^T-AuNps-CK inhibited the cell viability to 70.74 ± 1.24% while free drug inhibited the cell viability to 51.60 ± 3.68%, suggesting that the systemic cytotoxicity of CK in normal cell line (RAW264.7) was reduced in the nanoformulation. Whereas in cancer cell lines, DCY51^T-AuNps-CK exhibited slightly higher cytotoxicity in lung adenocarcinoma and colon adenocarcinoma cells compared to free drug starting at 5 µM of CK, which is considered to be non-toxic in normal cells (Figures 7A- C). Nonetheless, the ginsenoside CK utilized for this experiment did not exhibit any cytotoxicity towards cancer cells even at concentrations ≥10 mM. This irregularity must be addressed thoroughly prior to further experiments.

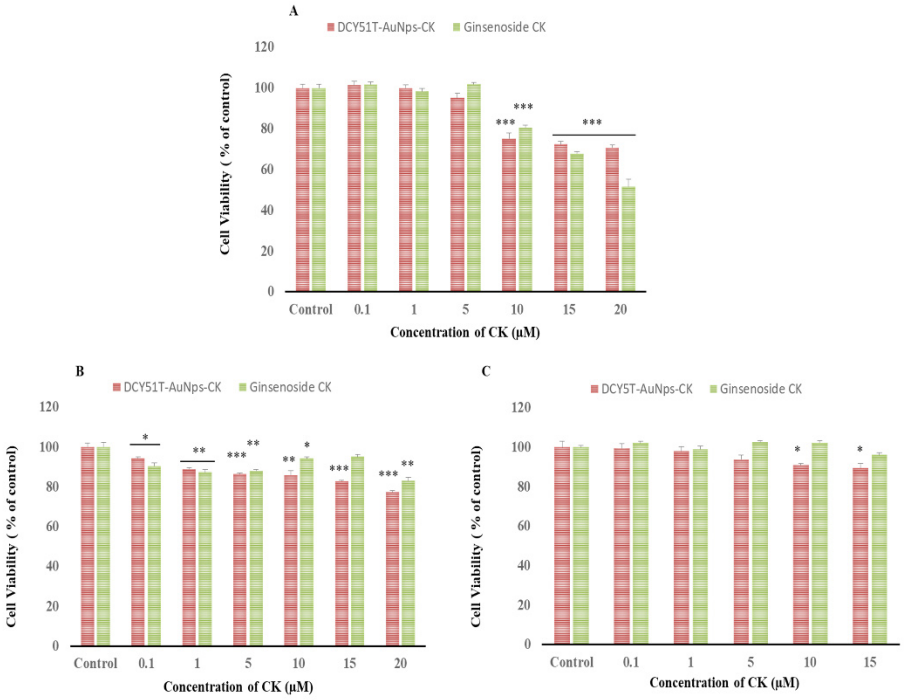

Figures 7(A-C): Cytotoxicity of DCY51^{T}-AuNps-CK and ginsenoside CK after 48 h of incubation. Macrophage cell line RAW264.7 **(A)**, lung cancer A549 **(B)**, and Colon cancer HT29 **(C)** cells.

For the following *in vitro* photothermal therapy experiment, the use of DCY51^{T}-AuNps-CK at 1 and 5 ppm (equivalent to 0.18 and 0.89 µM of CK) did not exert any apparent cytotoxicity within this concentration range and is regarded to be non-toxic and bio-inert towards normal and cancer cell lines.

In Vitro Photothermal Therapy and Apoptosis Detection

As the result of EPR effect, DCY51^{T}-AuNps-CK may accumulate in tumor tissues due to leaky vasculatures. Once accumulated, cationic DCY51^{T}-AuNps-CK may be uptaken inside the cells by receptor-independent endocytosis through interaction with the cell membrane [41]. Ginsenoside CK may then be released by lysosomal degrading enzymes, while DCY51^{T}-AuNps are expected to retain its stability in low acidic environment. In addition, DCY51^{T}-AuNps-CK can be irradiated at mild wavelength to rapidly induce cell lysis due to the elevated temperature induced by light to heat conversion (hyperthermia). Localized heat treatment utilizing temperatures over 40°C has been reported to irreversibly damage tumor cells by inducing protein degradation and DNA repair deficiency [51].

To investigate the photothermal effects of DCY51^{T}-AuNps-CK, an 800 nm laser at a heat flux density of 0.74 W/cm^2 was used to irradiate normal cell (RAW264.7) and cancer cell (A549 and HT29) lines (Figure 8).

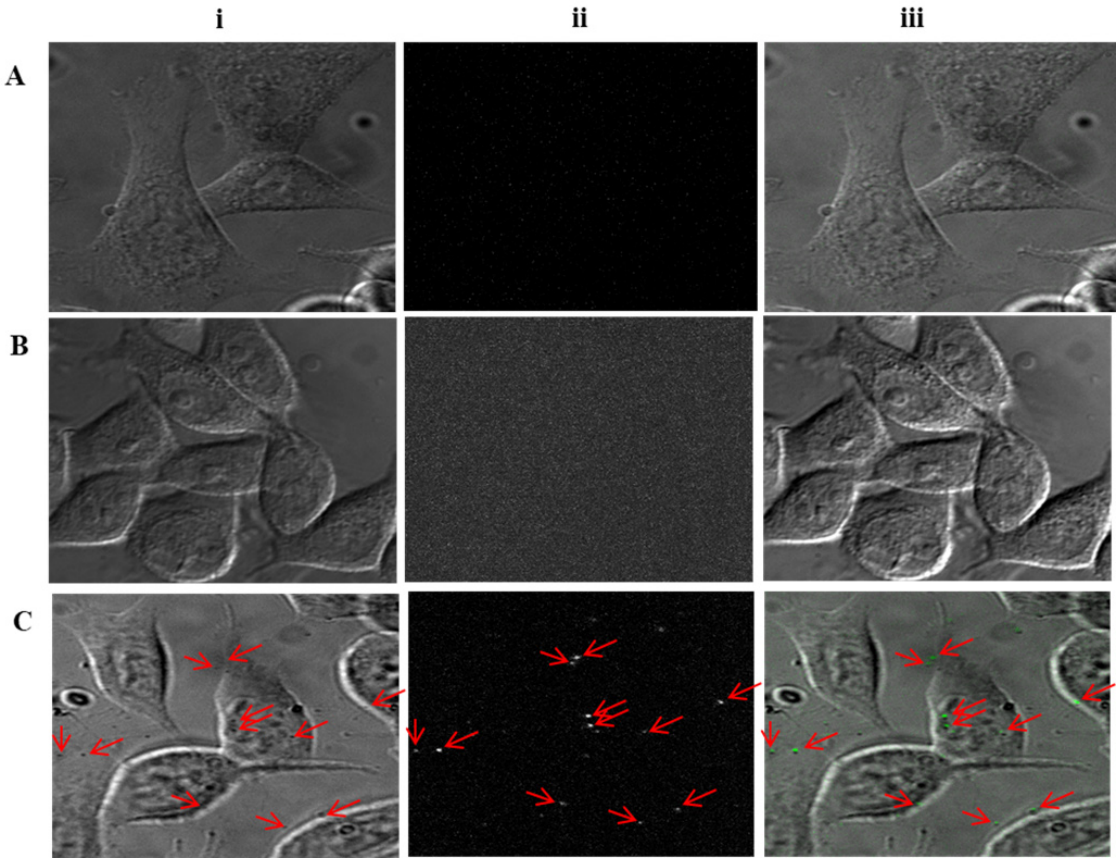

Figure 8: Detection of intercellular AuCK/Exosome in the Stomach cancer cell lines (AGS). **A**: Control, **B**: 800nm Laser treatment for 10min., C: AuCKNP/Exosome + Laser at 800nm for 10min.

These cells were incubated with DCY51^{T}-AuNps or DCY51^{T}-AuNps-CK for 48 h and then irradiated directly above the cell plates for 10 min with a laser spot size of 0.2 cm^2, resulting in a total energy dose of 88.80 J (Figures 9 A-C). To specifically analyze the photothermal effects, Hoechst staining was applied (Figure S6). As shown in Figure 9, fluorescent images showed that the blank group, which was irradiated with laser treatment alone, exhibited no change in the cell apoptosis. As predicted, incubation with DCY51^{T}-AuNps (negative control) induced slight apoptosis in normal and cancer cells since they caused cell inhibition within this concentration range as demonstrated by MTT results (Figures 9B, C, D).

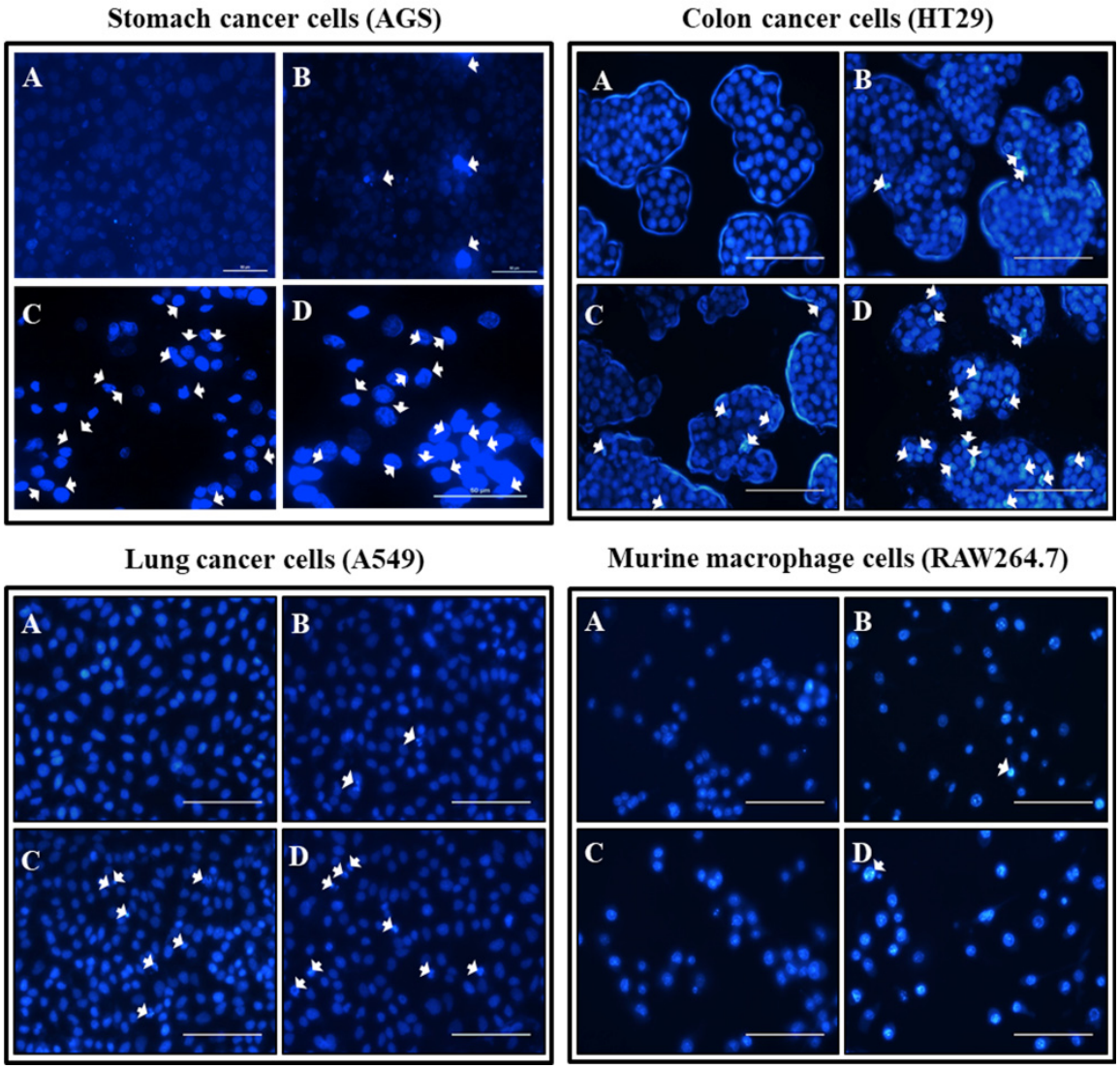

Figures 9(A-D): Fluorescent images of cells stained with Hoechst stain. Blank **(A)**, DCY51^{T}-AuNps; 0.5 ppm **(B)**. DCY51^{T}-AuNps-CK; 1 ppm **(C)**, DCY51^{T}-AuNps-CK; 5 ppm **(D)**. Apoptotic cells are indicated with white arrows; scale bar 10 µm; incubation time 48 h. There were more apoptotic cells in the DCY51^{T}-AuNps-CK groups than in blank or in the negative control (DCY51^{T}-AuNps). The co-treatment groups of hyperthermia and chemotherapy exhibited the greatest number of apoptosis in cancer cells.

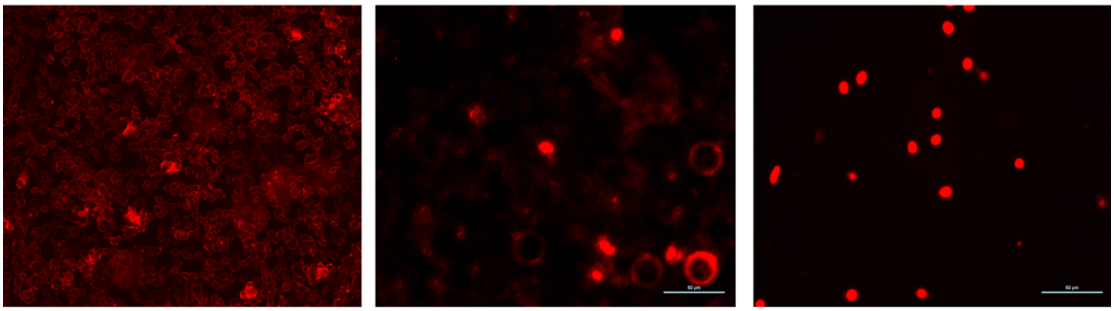

Figure S6: Apoptosis. PI staining.

However, the number of apoptotic cells in the DCY51^{T}-AuNps-CK groups was significantly higher than those in the DCY51^{T}-AuNps groups after photothermal therapy. Moreover, based on these preliminary *in vitro* results, cells incubated with DCY51^{T}-AuNps-CK after 48 h were shown to demonstrate higher apoptosis in lung and colon adenocarcinoma cells than normal cells. Increasing the concentration of DCY51^{T}-AuNps-CK from 1 to 5 ppm also resulted in higher apoptotic cells in cancer cell lines. This finding suggests that DCY51^{T}-AuNps-CK have the potential to increase apoptosis in cancer cells in conjunction with photo-induced hyperthermia than chemotherapy alone, possibly due to the increased sensitivity of tumor cells to ginsenoside or light-triggered drug release into cancer cells (51-53]. The proposed mechanism of cell internalization of DCY51^{T}-AuNps-CK by EPR effect and *in vitro* photothermal therapy is demonstrated in Figure 10.

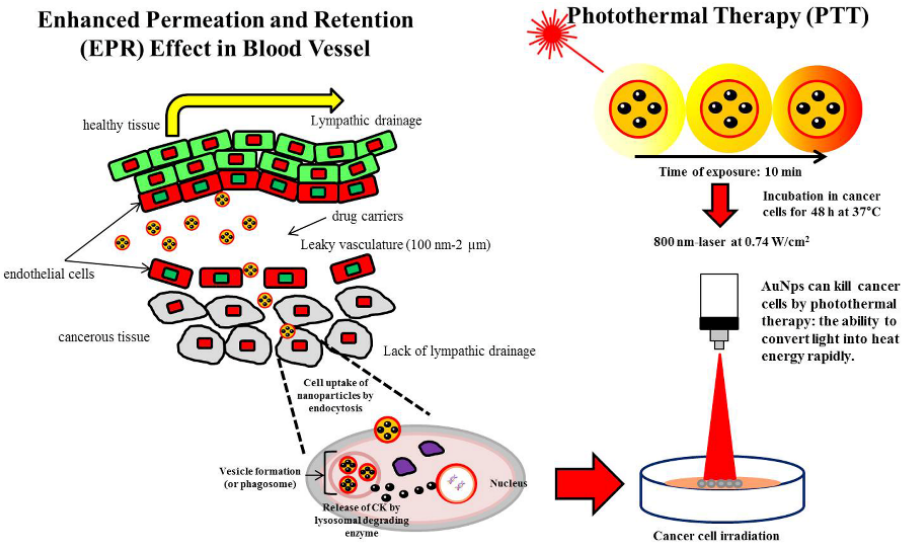

Figure 10: The proposed mechanism of cell internalization of DCY51^{T}-AuNps-CK by EPR effect and *in vitro* photothermal therapy. DCY51^{T}-AuNps-CK reaches the cell membrane by exploiting the property of EPR effect. Following association with cell by endocytosis, DCY51^{T}-AuNps-CK may aggregate on the anionic surface of cancer cells due to the cationic surface charge of nanoparticles. In conjunction, DCY51^{T}-AuNps-CK can be irradiated to rapidly induce cell lysis.

Several studies have reported that when conjugated with drugs, AuNps can function as drug carriers to enhance the release and uptake of drug to tumor tissues by hyperthermia stimulation [54]. Despite the lower toxicity of AuNps compared with other metallic nanoparticles, their lack of clearance from the body still remains an issue [54]. Specific targeting of cancer cells and minimizing the risk of *in vivo* toxicity are the main challenges of this study and must be thoroughly addressed prior to *in vivo* experiments [55].

Conclusion

In summary, this study highlights the development of ginsenoside nanocarriers by DCY51^T-AuNps-CK. DCY51^T-AuNps-CK were synthesized by one-pot biosynthesis by *L. kimchicus* DCY51^T. Ginsenoside CK was effectively loaded into gold nanocarriers by non-covalent conjugation. The synthesized metal nanocarriers were characterized by UV-Vis spectroscopy, FE-TEM, XRD, FTIR, DLS, TGA, and DSC. The drug loading efficiency was evaluated by LC-MS. The FTIR spectra of DCY51^T-AuNps-CK confirmed the presence of functional groups which belonged to ginsenosides. Ginsenoside loading results in smaller nanoparticles probably due to supplementary reduction and stabilization of gold atoms by self-assembled monolayer of ginsenoside CK, curtailing nanoparticle growth by aggregation. *In vitro* stability of DCY51^T-AuNps-CK demonstrated their resistance to aggregation and dissociation caused by pH variation or a high ionic strength environment. Preferential cytotoxicity of DCY51^T-AuNps-CK against lung adenocarcinoma cells and colon adenocarcinoma cells than DCY51^T-AuNps was demonstrated by MTT assay. Increased apoptosis of DCY51^T-AuNps-CK in cancer cells at sublethal concentration (1 and 5 µg/mL) was confirmed by *in vitro* photothermal therapy with excitations by laser at a mild wavelength. These results suggest that DCY51^T-AuNps-CK are promising drug deliver platforms for cancer therapy as novel photothermal and chemotherapeutic agents.

Acknowledgements

This work was supported by Nano Conversion Foundation funded by the Ministry of Science and ICT (MSIT, Korea) & the Ministry of Trade, Industry and Energy (MOTIE, Korea) [Project No. R201800510].

References

1. Kim DH (2017) Gut microbiota-mediated pharmacokinetics of ginseng saponins. J Ginseng Res: 1-9.
2. Kim YJ, Zhang D, Yang DC (2015) Biosynthesis and biotechnological production of ginsenosides. Biotechnol Adv 33: 717-735.
3. Wong AS, Che CM, Leung KW (2015) Recent advances in ginseng as cancer therapeutics: a functional and mechanistic overview. Nat Prod Rep 32: 256-272.
4. Kim DH (2009) Metabolism of Ginsenosides to Bioactive Compounds by Intestinal Microflora and Its Industrial Application. J Ginseng Res 33: 165-176.
5. Mathiyalagan R, Subramaniyam S, Kim YJ, Kim YC, Yang DC (2014) Ginsenoside compound K-bearing glycol chitosan conjugates: synthesis, physicochemical characterization, and *in vitro* biological studies. Carbohydrate polymers 112: 359-366.
6. Voruganti S, Qin JJ, Sarkar S, Nag S, Walbi IA, et al. (2015) Oral nanodelivery of anticancer ginsenoside 25-OCH_3-PPD, a natural inhibitor of the MDM2 oncogene: Nanoparticle preparation, characterization, *in vitro* and *in vivo* anti-prostate cancer activity, and mechanisms of action. Oncotarget. 6: 21379-21394.
7. Yang ZS, Gao J, Wang T, Yin Y, Teng B, et al. (2011) Enhancement of Oral Bioavailability of 20(S)-Ginsenoside Rh2 through Improved Understanding of Its Absorption and Efflux Mechanisms. Drug Metab Dispos 39: 1866-1872.
8. Liang ZQ, Srinivasan S, Kim YJ, Kim HB, Wang HT, et al. (2011) *Lactobacillus kimchicus* sp. *nov*., a β-glucosidase-producing bacterium isolated from kimchi. Int. J. Syst. Evol. Microbiol 61: 894-897.
9. Chenna R, Sugawara H, Koike T, Lopez R, Gibson TJ, et al. (2003) Multiple sequence alignment with the Clustal series of programs. Nucleic Acids Res 31: 3497-3500.
10. Singh P, Kim YJ, Wang C, Mathiyalagan R, Yang D C (2016b) Microbial synthesis of Flower-shaped gold nanoparticles. Artif Cells Nanomed Biotechnol 44: 1469-1474.
11. Singh P, Singh H, Kim YJ, Mathiyalagan R, Wang C, et al. (2016c) Extracellular synthesis of silver and gold nanoparticles by *Sporosarcina koreensis* DC4 and their biological applications. Enzyme Microb Technol 86: 75-83.
12. Jukes TH, Kimura M (1984) Evolutionary constraints and the neutral theory. J Mol Evol 21: 90-92.
13. Tamura K, Stecher G, Peterson D, Filipski A, Kumar S (2013) MEGA6: Molecular Evolutionary Genetics Analysis Version 6.0. Mol Biol Evol 30: 2725-2729.
14. Markus J, Mathiyalagan R, Kim YJ, Abbai R, Singh P, et al. (2016) Intracellular Synthesis of Gold Nanoparticles with Antioxidant Activity by Probiotic *Lactobacillus kimchicus* DCY51^T Isolated From Korean Kimchi. Enzyme Microb Technol 95: 85-93.
15. Haiss W, Thanh NT, Aveyard J, Fernig DG (2007) Determination of Size and Concentration of Gold Nanoparticles from UV−Vis Spectra. Anal Chem. 79: 4215-4221.
16. Hu Y, Liu W, Wu F (2017) Novel multi-responsive polymer magnetic microgels with folate or methyltetrahydrofolate ligand as anticancer drug carriers. RSC Advances 7: 10333-10344.
17. Debnath R, Purkayastha DD, Hazra S, Ghosh NN, Bhattacharjee CR, et al. (2016) Biogenic synthesis of antioxidant, shape selective gold nanomaterials mediated by high altitude lichens. Mater Lett 169: 58-61.
18. Ramamurthy C, Padma M, Mareeswaran R, Suyavaran A, Kumar MS, et al. (2013) The extra cellular synthesis of gold and silver nanoparticles and their free radical scavenging and antibacterial properties. Coll Surf B Biointerfaces 102: 808-815.
19. Madhusudhan A, Reddy GB, Venkatesham M, Veerabhadram G, Kumar DA, et al. (2014) Efficient pH Dependent Drug Delivery to Target Cancer Cells by Gold Nanoparticles Capped with Carboxymethyl Chitosan. Int J Mol Sci 15: 8216-8234.
20. Tannock IF, Rotin D (1989) Acid pH in tumors and its potential for therapeutic exploitation. Cancer Res 49: 4373-4384.
21. Leonard K, Ahmmad B, Okamura H, Kurawaki J (2011) *In situ* green synthesis of biocompatible ginseng capped gold nanoparticles with remarkable stability. Coll Surf B Biointerfaces 82: 391-396.

22. Aceituno VC, Ahn S, Simu SY, Wang C, Mathiyalagan R, et al. (*2016*) Silver nanoparticles from *Dendropanax morbifera* Léveille inhibit cell migration, induce apoptosis, and increase generation of reactive oxygen species in A549 lung cancer cells. *In Vitro* Cellular & Developmen Bio Animal 52: 1012-1019.

23. Ahn S, Siddiqi MH, Aceituno VC, Simu SY, et al. (2016) Ginsenoside Rg5:Rk1 attenuates TNF-α/IFN-γ-induced production of thymus- and activation-regulated chemokine (TARC/CCL17) and LPS-induced NO production via downregulation of NF-κB/p38 MAPK/STAT1 signaling in human keratinocytes and macrophages. *In Vitro* Cellular & Developmen Bio Animal 52: 287-295.

24. Wang D, Markus J, Kim YJ, Wang C, Pérez ZEJ, et al. (2016b) Coalescence of functional gold and monodisperse silver nanoparticles mediated by black *Panax ginseng* Meyer root extract. Int J Nanomed 11: 6621-6634.

25. Lee SA, Kang SH (2014) Fluorescent-free detection on nanobiochips based on wavelength-dependent single plasmonic nanoparticles by differential interference contrast microscopy. Biosensors and Bioelectronics 60: 45-51.

26. Iravani S (2014) Bacteria in Nanoparticle Synthesis: Current Status and Future Prospects. Int Sch Res Notices 2014: 359316.

27. Korbekandi H, Iravani S, Abbasi S (2009) Production of nanoparticles using organisms. Crit Rev Biotechnol 29: 279-306.

28. Korbekandi H, Iravani S, Abbasi S (2012) Optimization of biological synthesis of silver nanoparticles using *Lactobacillus casei* subsp. *casei*. J Chem Technol Biotechnol 87: 932-937.

29. Nair B, Pradeep T (2002) Coalescence of Nanoclusters and Formation of Submicron Crystallites Assisted by *Lactobacillus* Strains. Cryst Growth Des 2: 293-298.

30. Markus J, Kim YJ, Wang C, Ahn S, Mathiyalagan R, Yang DC (2017) Biosynthesis, Characterization, and Bioactivities Evaluation of Silver and Gold Nanoparticles Mediated by the Roots of Chinese Herbal *Angelica pubescens* Maxim. Nanoscale Res Lett 12: 46.

31. Shedbalkar U, Singh R, Wadhwani S, Gaidhani S, Chopade B (2014) Microbial synthesis of gold nanoparticles: Current status and future prospects. Adv Coll Interface Sci 209: 40-48.

32. Banerjee UC (2013) Synthesis of Gold Nanoparticles Using Whole Cells of *Geotrichum candidum*. J Nanopart 2013: 150414.

33. Jazayeri MH, Amani H, Pourfatollah AA, Pazoki-Toroudi H, Sedighimoghaddam B (2016) Various methods of gold nanoparticles (GNPs) conjugation to antibodies. Sens Biosensing Res 9: 17-22.

34. Singh P, Singh H, Aceituno VC, Ahn S, Kim YJ, Yang DC (2017) Bovine serum albumin as a nanocarrier for the efficient delivery of ginsenoside compound K: preparation, physicochemical characterizations and *in vitro* biological studies. RSC Adv 7: 15397-15407.

35. Rahman S (2016) Size and Concentration Analysis of Gold Nanoparticles with Ultraviolet-Visible Spectroscopy. Undergrad. J Math Model. One Two 7.

36. Hoskins C, Min Y, Gueorguieva M, McDougall C, Volovick A, Pet al. (2012) Hybrid gold-iron oxide nanoparticles as a multifunctional platform for biomedical application. J Nanobiotechnol 10: 27.

37. Wang C, Mathiyalagan R, Kim YJ, Aceituno VC, Singh P, et al. (2016a) Rapid green synthesis of silver and gold nanoparticles using *Dendropanax morbifera* leaf extract and their anticancer activities. Int J Nanomed 11: 3691-3701.

38. Upadhyaya L, Singh J, Agarwal V, Pandey A, Verma SP, et al. (2015) Efficient water soluble nanostructured ZnO grafted O-carboxymethyl chitosan/curcumin-nanocomposite for cancer therapy. Process Biochem 50: 678-688.

39. Kishen A (2015) Current and Potential Clinical Applications. In. Nanotechnology in Endodontics. Springer.

40. Poon RT, Borys N (2009) Lyso-thermosensitive liposomal doxorubicin: a novel approach to enhance efficacy of thermal ablation of liver cancer. Expert Opin Pharmacother 10: 333-343.

41. Fröhlich E (2012) The role of surface charge in cellular uptake and cytotoxicity of medical nanoparticles. Int J Nanomed 7: 5577-5591.

42. Elbeshehy EK, Elazzazy AM, Aggelis G (2015) Silver nanoparticles synthesis mediated by new isolates of *Bacillus* spp., nanoparticle characterization and their activity against Bean Yellow Mosaic Virus and human pathogens. Front Microbiol 6: 453.

43. Araujo PM, Oliveira GB, Cordula CR, Leite EL, Carvalho, et al. (2004) Sulfated fucan as support for antibiotic immobilization. Braz J Med Biol Res 37: 301-305.

44. Kumar CS, Raja M, Sundar DS, Antoniraj MG, Ruckmani K (2015) Hyaluronic acid co-functionalized gold nanoparticle complex for the targeted delivery of metformin in the treatment of liver cancer (HepG2 cells). Carbohydr Polym 128: 63-74.

45. Roy S, Das TK, Maiti GP, Basu U (2016) Microbial biosynthesis of nontoxic gold nanoparticles. Mater Sci Eng B 203: 41-51.

46. Li P, Zhou X, Qu D, Guo M, Fan C, et al. (2017) Preliminary Study on Fabrication, Characterization and Synergistic Anti-Lung Cancer Effects of Self-Assembled Micelles of Covalently Conjugated Celastrol-Polyethylene Glycol-Ginsenoside Rh2. Drug Deliv 24: 834-845.

47. Gao Z, Su R, Huang R, Qi W, He Z (2014) Glucomannan-mediated facile synthesis of gold nanoparticles for catalytic reduction of 4-nitrophenol. Nanoscale Res Lett 9: 404.

48. Valko M, Leibfritz D, Moncol J, Cronin MT, Mazur M, et al. (2007) Free radicals and antioxidants in normal physiological functions and human disease. Int J Biochem Cell Biol 39: 44-84.

49. Bhattacharjee S (2016) DLS and zeta potential - What they are and what they are not? J Control Release 235: 337-351.

50. Ankrum JA, Miranda OR, Ng KS, Sarkar D, Xu C, et al. (2014) Engineering cells with intracellular agent-loaded microparticles to control cell phenotype. Nat Protoc 9: 233-245.

51. Zhang AW, Guo WH, Qi YF, Wang JZ, Ma XX, et al. (2016) Synergistic Effects of Gold Nanocages in Hyperthermia and Radiotherapy Treatment. Nanoscale Res Lett 11: 279.

52. Kautzka Z, Clement S, Goldys EM, Deng W (2017) Light-triggered liposomal cargo delivery platform incorporating photosensitizers and gold nanoparticles for enhanced singlet oxygen generation and increased cytotoxicity. Int J Nanomed 12: 969-977.

53. Yeo ELL, Joshua U, Cheah J, Neo DJH, Goh WI, et al. (2017) Exploiting the protein corona around gold nanorods for low-dose combined photothermal and photodynamic therapy. J Mater Chem B 5: 254-268.

54. Lee J, Chatterjee DK, Lee MH, Krishnan S (2014) Gold nanoparticles in breast cancer treatment: promise and potential pitfalls. Cancer Lett 347: 46-53.

55. Fischer HC, Chan WC (2007) Nanotoxicity: the growing need for *in vivo* study. Curr Opin Biotechnol 18: 565-571.